Nature Communications

https://doi.org/10.1038/s41467-026-70984-1

Article in Press

LSD1 inhibitor, TAS1440, disrupts INSM1-LSD1 complex activating tumor-suppressive pathways via transcriptional reprogramming in neuroendocrine SCLC

Received: 2 January 2025

Accepted: 9 March 2026

Cite this article as: Machida, T., Gong, Y., Tsukioka, S. *et al.* LSD1 inhibitor, TAS1440, disrupts INSM1-LSD1 complex activating tumor-suppressive pathways via transcriptional reprogramming in neuroendocrine SCLC. *Nat Commun* (2026). https://doi.org/10.1038/s41467-026-70984-1

Takumitsu Machida, Yingbo Gong, Sayaka Tsukioka, Atsushi Onodera, Akitoshi Nakayama, Naoko Hashimoto, Takahiro Fuchigami, Motoi Nishimura, Tomohiro Ogino, Ryota Kurimoto, Yasufumi Uematsu, Hidemi Suzuki, Hongye Yu, Mingyang Chen, Masataka Yokoyama, Ikki Sakuma, Yuki Taki, Takashi Kono, Takashi Miki, Shinichiro Motohashi, Yusuke Kawashima, Osamu Ohara, Satoshi Yamashita, Tatsuya Suzuki, Ryo Hatanaka, Yasuo Kodama, Shuichi Ohkubo & Tomoaki Tanaka

LSD1 Inhibitor, TAS1440, Disrupts INSM1-LSD1 Complex Activating Tumor-Suppressive Pathways via Transcriptional Reprogramming in Neuroendocrine SCLC

Takumitsu Machida[1, #], Yingbo Gong[2, #], Sayaka Tsukioka[1], Atsushi Onodera[3, 4], Akitoshi Nakayama[2], Naoko Hashimoto[2, 3], Takahiro Fuchigami[2], Motoi Nishimura[2], Tomohiro Ogino[3], Ryota Kurimoto[2], Yasufumi Uematsu[5], Hidemi Suzuki[5], Hongye Yu[2], Mingyang Chen[2], Masataka Yokoyama[2], Ikki Sakuma[2], Yuki Taki[2], Takashi Kono[2, 3], Takashi Miki[6], Shinichiro Motohashi[7], Yusuke Kawashima[8], Osamu Ohara[8], Satoshi Yamashita[1], Tatsuya Suzuki[1], Ryo Hatanaka[1], Yasuo Kodama[1], Shuichi Ohkubo[1, *], and Tomoaki Tanaka[2, 3, *]

Lead contact: Tomoaki Tanaka

*Correspondence: tomoaki@restaff.chiba-u.jp (T.T.); s-ohkubo@taiho.co.jp (S.O.)

[1] Discovery and Preclinical Research Division, Taiho Pharmaceutical Co., Ltd., 3 Okubo, Tsukuba, Ibaraki 300-2611, Japan

[2] Department of Molecular Diagnosis, Graduate School of Medicine, Chiba University, Chiba 260-8670, Japan

[3] Research Institute of Disaster Medicine (RIDM), Chiba University, Chiba 260-8670, Japan

[4] Institute for Advanced Academic Research, Chiba University, Chiba 263-8522, Japan

[5] Department of General Thoracic Surgery, Graduate School of Medicine, Chiba University, Chiba 260-8670, Japan

[6] Department of Medical Physiology, Graduate School of Medicine, Chiba University, Chiba 260-8670, Japan

[7] Department of Medical Immunology, Graduate School of Medicine, Chiba University, Chiba 260-8670, Japan

[8] Department of Applied Genomics, Kazusa DNA Research Institute, Kisarazu, Chiba 292-0818, Japan

[#]These authors contributed equally

Abstract

Small cell lung cancer (SCLC) is aggressive with limited treatment options, requiring new therapies. Lysine-specific histone demethylase 1A (LSD1) maintains neuroendocrine state by repressing NOTCH/TGF-β signaling; their reactivation suppresses proliferation and induces differentiation. However, mechanisms of LSD1 inhibition and chemoresistance remain unclear. Here we developed TAS1440, a histone H3-competitive LSD1 inhibitor, using structure-based engineering to improve specificity and reduce off-target effects. Unlike irreversible inhibitors targeting the flavin adenine dinucleotide site, TAS1440 non-covalently targets the H3-binding pocket to enhance safety and efficacy. TAS1440 suppressed proliferation in INSM1/ASCL1-high SCLC-A cells and induced tumor regression in xenografts. TAS1440 acts through dual mechanisms: inhibiting LSD1 activity and disrupting LSD1-repressive complexes, remodeling histone marks and activating transcription factors INSM1 and SMAD2. These actions reprogram tumor-suppressive TGF-β/NOTCH signaling, supporting TAS1440 as epigenetic therapy for SCLC. Loss of LSD1 enzymatic activity or INSM1 knockout abrogated TAS1440 effects, defining its mode of action and chemoresistance. These findings support TAS1440 as a next-generation epigenetic therapy candidate for INSM1-high SCLC-A.

Introduction

Small-cell lung cancer (SCLC) is an aggressive, high-grade neuroendocrine carcinoma with a poor prognosis. It characteristically expresses neuroendocrine markers, including achaete-scute homolog 1 (ASCL1), neurogenic differentiation 1 (NEUROD1), and insulinoma-associated protein 1 (INSM1)[1]. First-line platinum-based chemotherapy is initially effective; however, relapse is common, and the 5-year survival rate remains <7%[2], underscoring the need for new therapeutic strategies. Contemporary transcriptomic frameworks delineate SCLC into ASCL1- (SCLC-A), NEUROD1- (SCLC-N), and POU2F3-driven (SCLC-P) states, with an inflamed SCLC-I state being increasingly recognized[3,4]. Among tumor-suppressive circuits silenced in SCLC, NOTCH signaling—central to cell-fate decisions—functions as a tumor suppressor: its loss sustains the neuroendocrine phenotype and promotes lineage plasticity and progression[5], whereas NOTCH reactivation in preclinical models suppresses proliferation, induces cell death, and drives transdifferentiation toward non-neuroendocrine states[6]. Therefore, NOTCH repression constitutes a fundamental vulnerability, particularly in neuroendocrine-high SCLC-A.

As a strategy to restore NOTCH signaling, lysine-specific demethylase 1A (LSD1/KDM1A)—a flavin-dependent amine oxidase and epigenetic regulator—has emerged as a promising therapeutic target in SCLC. LSD1 represses NOTCH-associated genes predominantly by demethylating histone H3 lysine 4 (H3K4me1/2)[7], thereby shaping chromatin states and transcriptional output. LSD1 requires flavin adenine dinucleotide (FAD) for its enzymatic activity and supports transcriptional repression via H3K4 demethylation[8]. Notably, LSD1 functions within multi-protein corepressor assemblies, including the REST corepressor (CoREST)[9] and the nucleosome remodeling and deacetylase (NuRD) complex[10].

Elevated LSD1 expression is observed across multiple cancers, including SCLC, where its activity is associated with proliferation, differentiation, and epithelial–mesenchymal transition[11]. Pharmacological inhibition of LSD1 activates NOTCH signaling and downregulates neuroendocrine-associated genes such as ASCL1, suppressing SCLC cell proliferation *in vitro* and demonstrating antitumor efficacy in mouse xenograft models[12]. Nonetheless, the detailed mechanisms by which LSD1 inhibitors act in SCLC, and the determinants of therapeutic resistance, remain incompletely defined—motivating further development of next-generation inhibitors and mechanistic dissection.

LSD1 inhibitors are broadly classified as covalent FAD-directed agents and non-covalent chemotypes that compete at the histone H3-binding pocket[13]. Covalent inhibitors such as ORY-1001 and GSK2879552 irreversibly modify the FAD cofactor to block catalysis[14]; however, irreversible binding raises concerns about off-target effects, limited adaptability for rapidly turning-over enzymes, and potential immunogenicity[4,13,15]. In contrast, non-covalent inhibitors such as CC-90011[16] compete with histone H3 at its binding site, enabling improved selectivity, tunable pharmacokinetics, and potentially wider therapeutic windows; importantly, they can also perturb protein–protein interactions within LSD1 complexes, suggesting mechanistic distinctions from covalent agents that extend beyond enzyme inhibition[13,17].

Here, we report TAS1440, a potent histone H3–competitive non-covalent LSD1 inhibitor, which showed a favorable selectivity profile in our preclinical assays. TAS1440 exhibited preferential activity in SCLC-A models. Mechanistically, our data support a dual mode of action: (i) direct inhibition of LSD1 catalytic activity, remodeling the chromatin landscape via altered H3 methylation, and (ii) disruption of LSD1-containing repressive complexes (e.g., CoREST and NuRD), relieving INSM1-tethered repression and enhancing SMAD2-dependent signaling.

Together, these effects reprogram transcriptional networks in tumor-suppressive pathways, including TGF-β and NOTCH, supporting TAS1440 as a potential therapeutic candidate for SCLC—particularly the SCLC-A subtype characterized by high INSM1 expression.

Results

Molecular Subtype-Driven Therapeutic Vulnerabilities in SCLC: TAS1440 as a Selective LSD1 Inhibitor for SCLC-A

SCLC is a rapidly growing tumor with poor prognosis and limited treatment options. SCLC comprises transcriptionally defined states with distinct vulnerabilities. We profiled 22 SCLC cell lines by bulk RNA sequencing (RNA-seq) to stratify models by subtype signatures and lineage-defining transcription factors (Fig. 1a). Consistent with previous reports[1], our cluster analysis classified the cell lines into four molecular states annotated by *ASCL1* (SCLC-A), *NEUROD1* (SCLC-N), *POU2F3* (SCLC-P), and a *YAP1*-high group (Fig. 1b–d). As expected, SCLC-A lines showed higher expression of neuroendocrine markers (e.g., *INSM1*, *DLL3*), as well as genes enriched in SCLC-A (e.g., *SYK*, *ETS2*, *CRACDL*); moreover, *ASCL1* expression was the highest in SCLC-A (Fig. 1e). These findings highlight the molecular heterogeneity of SCLC and the distinct transcriptional characteristics that may underlie differential responsiveness to LSD1-regulated programs.

Given reports that *YAP1*-high lines are frequently misclassified (e.g., *SMARCA4*-deficient undifferentiated tumors or sarcomatoid neoplasms[3,4]) and are not considered a consensus SCLC subtype, we examined our dataset and confirmed markedly reduced *SMARCA4* expression in these

lines (Fig. 1e). To avoid confounding in downstream analyses, we excluded these models and re-analyzed the remaining 19 SCLC lines, which retained the SCLC-A/N/P assignments (Supplementary Fig. 1a–d). This 19-line framework provided a robust platform for evaluating LSD1-regulated transcriptional programs and therapeutic vulnerabilities.

To evaluate the effects of LSD1 inhibitors across SCLC subtypes, we profiled TAS1440 and two covalent inhibitors (ORY-1001 and GSK2879552) in 19 SCLC cell lines using single-concentration challenge at 7,500 nM to assess drug resistance, with cell growth expressed as % of DMSO control (Fig. 2a, b). Across subtypes, TAS1440 showed the strongest growth suppression in SCLC-A (Fig. 2a, b), highlighting it as a promising agent for neuroendocrine-high disease.

Within SCLC-A, NCI-H1417, NCI-H510A, NCI-H146, and COR-L51 were particularly sensitive to TAS1440 and displayed steep dose–response curves relative to other SCLC-A lines or subtypes (Fig. 2c and Supplementary Fig. 2a). Consistent with these responses, these lines yielded the lowest TAS1440 IC_{50} values in the panel, whereas the covalent comparators frequently showed $IC_{50} \geq 1{,}000$ nM and were often right-censored at the upper testing limit (7,500 nM) (Fig. 2d and Supplementary Fig. 2b). To benchmark TAS1440 against reversible, non-covalent inhibitors, we compared it with SP2509[18] and CC-90011[16] across the same panel (Supplementary Fig. 3). TAS1440 and CC-90011 (both H3-competitive) showed broadly similar inhibition patterns, with TAS1440 exhibiting greater potency in the most sensitive lines; in contrast, SP2509 produced broad cytotoxicity at higher concentrations, consistent with reported off-target liabilities (Supplementary Fig. 3).

TAS1440 is a small-molecule LSD1 inhibitor with a [1,1':2',1"-terphenyl]-4'-carboxamide scaffold (Fig. 2e) and a defined synthetic route (Supplementary Fig. 4a). Unlike tranylcypromine (TCP) analogs such as ORY-1001 and GSK2879552, which covalently modify the FAD cofactor, TAS1440 functions as a histone H3-competitive inhibitor. In biochemical assays, TAS1440 showed marked selectivity for LSD1 (IC_{50} = 4.8 nM) over related amine oxidases (LSD2, MAO-A, MAO-B; all IC_{50} > 10,000 nM; Fig. 2f) and a broader panel of epigenetic enzymes (e.g., JARID1A, DNMT1, EZH1/EED/SUZ12, HDAC1, JMJD2B/3, PRMT4; all IC_{50} > 10,000 nM; Supplementary Fig. 4b), indicating a favorable selectivity profile.

Consistent with classical competitive inhibition at the histone-substrate site, the apparent IC_{50} of TAS1440 for LSD1 increased as the H3K4me1 peptide concentration increased (e.g., 100 nM vs. 2,000 nM substrate), whereas ORY-1001 remained essentially substrate-insensitive (Fig. 2g). These biochemical findings are consistent with structural data presented later, where TAS1440 engages the H3-binding pocket of LSD1.

TAS1440 Modulates Global Gene Expression and Activates Tumor-Suppressive Pathways in SCLC

The potent inhibitory effects of TAS1440 in SCLC-A are likely dependent on LSD1-regulated neuroendocrine programs driven by lineage-defining factors such as *ASCL1* and *INSM1*. To characterize TAS1440-induced transcriptional changes, we performed bulk RNA-seq across 19 SCLC cell lines, comparing TAS1440-sensitive and -insensitive groups (Fig. 3a). In the TAS1440-sensitive NCI-H1417 cell line, 1017 genes were upregulated, whereas ≤500 genes were upregulated in insensitive lines (Fig. 3a, b). At baseline, *KDM1A/LSD1* expression was

considerably higher in the insensitive group than in the sensitive group across all SCLC lines and within SCLC-A (Fig. 3c), suggesting that elevated LSD1 abundance may diminish effective target engagement given that TAS1440 competes at the histone H3-binding pocket.

To link these transcriptional changes with growth-inhibitory effects, we correlated gene-wise $\log_2$(fold-change) (TAS1440 vs. DMSO) with cell growth (% of DMSO) across the 19 lines (Pearson correlation coefficient $|R| \geq 0.5$, $P < 0.05$). This analysis identified 207 genes with strong correlations ($|R| \geq 0.5$; $P < 0.05$), with the top 100 genes averaging a correlation coefficient of more than 0.5 (Fig. 3e and Supplementary Fig. 5a–c). TGF-β-related genes—including *SMAD6*, *BMP5*, *FBN1*, and *TGFB2*—were positively correlated with TAS1440 efficacy (i.e., more up-regulated with stronger growth inhibition), whereas neuroendocrine/ASCL1-axis genes such as *DLL3*, *INSM1*, and *ASCL1* showed negative correlations (i.e., more down-regulated with stronger growth inhibition) (Fig. 3f). Consistently, pathway-level gene-set enrichment analysis (GSEA) demonstrated higher normalized enrichment scores for NOTCH signaling in TAS1440-sensitive lines—both across all SCLC models and within the SCLC-A subset—further linking NOTCH activation to drug response (Fig. 3d). Collectively, these findings demonstrate that TAS1440 induces a coordinated reprogramming of gene expression, characterized by activation of NOTCH/TGF-β pathways and suppression of the neuroendocrine program, which collectively underlie its antiproliferative activity.

TGF-β and NOTCH Pathway Activation by TAS1440 Mediates Antitumor Effects in SCLC-A

To define the temporal dynamics of TAS1440-induced transcriptional rewiring, we performed RNA-seq in three TAS1440-sensitive SCLC-A lines, using full time courses in NCI-H1417 and

NCI-H146 (days 0, 1, 2, 3, 5, and 7) and a baseline/endpoint design in NCI-H510A (days 0 and 7). Global expression changes were modest on days 1–3 and became most pronounced by days 5–7 (Fig. 4a and Supplementary Fig. 6a). Kyoto Encyclopedia of Genes and Genomes (KEGG) pathway and GSEA consistently showed activation of tumor-suppressive programs—most notably TGF-β and NOTCH—with peak enrichment at later time points (Fig. 4b, f; Supplementary Fig. 6b, f; and Supplementary Fig. 7b). Concordantly, TAS1440 upregulated key pathway components and targets (e.g., *NOTCH1/3*, *JAG1*, *TGFB2*, *SMAD3/6*, *HES1*) (Fig. 4a and Supplementary Fig. 6a and Supplementary Fig. 7a). Pathways associated with neuroendocrine phenotypes[1], such as those observed in pancreatic and prostate cancer, were enriched among genes upregulated by TAS1440 treatment (Fig. 4b and Supplementary Fig. 6b).

At the protein level, TAS1440 rapidly induced SMAD2 phosphorylation, peaking around 30–45 min in NCI-H1417 and NCI-H146 (Fig. 4c; Supplementary Fig. 6c). Additionally, NOTCH1 expression increased more slowly, peaking at 3 days post-treatment in both models (Fig. 4c and Supplementary Fig. 6c).

Immunocytochemistry confirmed increased nuclear p-SMAD2 across all three models (Fig. 4d, Supplementary Fig. 6d, and Supplementary Fig. 7c) and enhanced nuclear accumulation of the NOTCH intracellular domain (NICD) (Fig. 4e, Supplementary Fig. 6e, and Supplementary Fig. 7d). These findings indicate TAS1440's ability to modulate global gene expression and activate tumor-suppressive pathways, particularly through engagement of TGF-β and NOTCH signaling[19,20], underscoring its therapeutic potential in SCLC-A.

To test pathway dependence, we perturbed each axis pharmacologically and genetically. The NOTCH inhibitor LY411575, the TGF-β inhibitor SB431542, and *SMAD2* siRNA (si*SMAD2*)

partially reversed TAS1440-mediated growth inhibition, whereas dual inhibition nearly abrogated the antiproliferative effect (Fig. 4g, Supplementary Fig. 6g, and Supplementary Fig. 7e). LY411575 attenuated TAS1440-induced *NOTCH1/HES1* upregulation, and SMAD2 knockdown blunted *HES1*, *TGFB2*, and *TGFBR2* induction across three cell lines (Fig. 4h, Supplementary Fig. 6h, and Supplementary Fig. 7f). To corroborate these pharmacologic findings at the transcriptome level, we performed RNA-seq analysis on *SMAD2*-knockdown NCI-H1417 and NCI-H146 cells following TAS1440 treatment (Supplementary Fig. 8). SMAD2 depletion was verified by reduced *SMAD2* FPKM in both models (Supplementary Fig. 8a). Relative to si*NC*, si*SMAD2* cells displayed substantially fewer TAS1440-responsive differentially expressed genes (DEGs), and a blunted global signature by heatmap (Supplementary Fig. 8b–d). Importantly, KEGG TGF-β signaling was no longer strongly enriched under si*SMAD2*, with dampened induction of canonical components (e.g., *TGFB2, TGFBR2*, *SMAD6/7*, *ID1/3*) (Supplementary Fig. 8e, f), indicating that SMAD2 is required for the full TGF-β program elicited by TAS1440.

Finally, comparison with four LSD1 inhibitors (ORY-1001, GSK2879552, CC-90011, and SP2509) showed that TAS1440 induced more pronounced genome-wide expression changes (Fig. 4i and Supplementary Fig. 6i) and stronger activation of p-SMAD2 and NOTCH1/NICD than comparators at the tested concentrations and time points (Fig. 4j, k; Supplementary Fig. 6j; and Supplementary Fig. 7g). While such cross-compound comparisons in cell-based systems are limited by differences in antiproliferative potency (IC_{50}) and potential variations in mechanism of action, these findings highlight TAS1440's distinctive capacity—as an H3-competitive LSD1 inhibitor—to activate TGF-β/NOTCH programs and suppress growth in SCLC-A.

TAS1440 Attenuates Neuroendocrine Identity and Modulates Immune-Related and Surface Antigen Pathways

Given that LSD1 blockade can restore MHC-I antigen presentation and enhance intrinsic immunogenicity, with NOTCH-linked attenuation of neuroendocrine features in SCLC[21], we evaluated whether TAS1440 modulates lineage identity and immune/surface-antigen programs across SCLC models. TAS1440 consistently suppressed *ASCL1* and the neuroendocrine (NE) marker *INSM1* in SCLC-A lines (*ASCL1*: Supplementary Fig. 9a; *INSM1*: Fig. 3f), whereas *NEUROD1*, *YAP1*, and *POU2F3* remained largely unchanged (Supplementary Fig. 9a). Sample–sample correlation matrices and lineage-marker profiles did not support transitions to SCLC-N, -P, or -Y (Supplementary Fig. 9b, c), indicating a loss of NE identity without subtype switching.

We next assessed the immunomodulatory effects of TAS1440. Across 19 lines, TAS1440 induced selective immunogenic rewiring: transcripts encoding MHC-I/antigen-processing components (*B2M*, *TAP1/2*, *HLA-A/B/C*) and IFN-γ–response genes (*IRF1*, *STAT1*, *CXCL9*/10) were upregulated, while *CD274/PD-L1* decreased (Supplementary Fig. 9d). GSEA revealed enrichment of NOTCH, JAK–STAT, and innate inflammatory pathways in a subset of lines (Supplementary Fig. 9f); however, these pathway changes did not consistently correlate with growth inhibition (the cell-growth vs. DMSO (%) indicator in Supplementary Fig. 9d, f), consistent with context-dependent pharmacodynamics in cell line systems.

Regarding clinically actionable antigens, TAS1440 downregulated *DLL3*−the target of the T-cell engager tarlatamab—while leaving *SEZ6*, *CD276 (B7-H3)*, and *TACSTD2* (*TROP2*) largely unchanged (Supplementary Fig. 9e). In ASCL1-expressing SCLC-A lines, TAS1440-induced NOTCH pathway enrichment negatively correlated with *ASCL1* and *DLL3* expression changes

indicating NOTCH-linked repression of the ASCL1–DLL3 axis (Supplementary Fig. 9g). These transcript-level findings suggest caution with concurrent DLL3-directed approaches (e.g., tarlatamab) but support antibody-drug conjugate (ADC) strategies targeting SEZ6, B7-H3, or TROP2 during TAS1440 exposure. Future confirmation will require cell-surface protein quantification (e.g., flow cytometry/proteomics) and validation in orthotopic/PDX models and, where feasible, clinical cohorts.

Dual Mechanisms of TAS1440 in SCLC-A: Inhibition of LSD1 Catalysis and Disruption of INSM1–LSD1 and SMAD2–LSD1 Complexes

To elucidate the multifaceted roles of the LSD1 complex in SCLC and the basis for differential responses to LSD1 inhibitors, we profiled LSD1-interacting proteins with or without inhibitors. NCI-H1417 cells were transfected with a 3×FLAG–Myc-tagged human LSD1 vector or an empty vector; after 46 h, cells were treated for 2 h with 0.1% DMSO or 300 nM LSD1 inhibitors (TAS1440, ORY-1001, GSK2879552) and subjected to FLAG immunoprecipitation followed by liquid chromatography–tandem mass spectrometry (LC-MS/MS) (Fig. 5a). In untreated cells, we identified 422 nuclear and 67 epigenetic factors bound to LSD1 (Fig. 5b). Enrichment analysis highlighted HDAC-containing corepressor complexes (e.g., CoREST-HDAC, NuRD, HCF-1, ALL-1 supercomplex) among LSD1 interactors (Supplementary Fig. 10a). Following TAS1440 treatment, 498 nuclear and 77 epigenetic factors were recovered (Fig. 5b, right). Similarly, 455/70 and 442/66 interactors were identified following ORY-1001 and GSK2879552 treatment, respectively (Supplementary Fig. 10b).

Quantitative interactome analysis revealed that TAS1440 caused dissociation of 78 nuclear factors (13 epigenetic) from LSD1 (Fig. 5c, red), while 344 (54) remained stable (Fig. 5c). Dissociated proteins included transcription factors (e.g., INSM1, SOX2, SMAD2) and chromatin modifiers (e.g., CHD4, SMARCA2) (Fig. 5c, d). RCOR1 binding was largely unchanged, whereas HDAC1 (and to a lesser extent, HDAC2) binding decreased; this result is consistent with immunoblot validation (Fig. 5e, f). ORY-1001 and GSK2879552 induced dissociation of 90 (12) and 87 (18) nuclear factors, respectively (Fig. 5d, Supplementary Fig. 10c–e). Across inhibitors, 35 proteins were commonly dissociated, whereas 22, including INSM1 and SMAD2, were TAS1440-specific (Supplementary Fig. 10f).

Co-immunoprecipitation and immunoblotting confirmed robust TAS1440-mediated INSM1 dissociation (mean ± SD; $P < 0.01$), exceeding other inhibitors (Fig. 5e, f). Dose–response analyses showed progressive loss of the INSM1–LSD1 interaction with increasing TAS1440 concentrations (Supplementary Fig. 10g, h), and at ≥300 nM, TAS1440 caused stronger INSM1 dissociation than other compounds (Supplementary Fig. 10i, j). TAS1440 also more strongly dissociated SMAD2 than comparators, consistent with downstream SMAD2 activation (Fig. 5d–f, Fig. 4j, Supplementary Fig. 6j, and Supplementary Fig. 7g).

To explore structural underpinnings, we performed molecular docking simulation using the LSD1–FAD complex (PDB: 2HKO) (Fig. 5g). Across replicate runs and scoring functions, TAS1440 consistently achieved more favorable docking scores (−10.1 kcal/mol) than comparators and adopted a pose along the histone H3–binding channel proximal to FAD, positioning its core within the substrate tunnel. To relate the small-molecule pocket to repressor engagement, we applied AlphaFold3 modeling to map partner-binding interfaces on LSD1 (Fig. 5h). In these models, the

TAS1440-defined pocket lies adjacent to regions predicted to engage INSM1 and SMAD2, providing a structural rationale for the observed dissociation of these factors from LSD1 upon TAS1440 treatment. While these predictions are computational, they converge with our biochemical and proteomic readouts.

Finally, X-ray co-crystal analysis shows occupancy of the H3-binding site *in vitro* (Fig. 5i), consistent with the substrate-competition observed in Fig. 2g. Furthermore, a comparison with the previously reported LSD1–CC-90011 structure (PDB: 6W4K)[16], another non-covalent H3-competitive inhibitor, demonstrates that TAS1440 and CC-90011 occupy nearly identical regions within this substrate-binding pocket, supporting a common mechanism. Superposition with LSD1–GSK2879552 (PDB: 6NQU) and an LSD1–INSM1 peptide complex (PDB: 3ZMS) shows that TAS1440 overlaps the H3 pocket and sterically intersects the INSM1 footprint, providing a direct steric basis for destabilizing the LSD1–INSM1 interaction. By contrast, GSK2879552 forms a covalent adduct with FAD at a shifted position that minimally overlaps the INSM1 site, consistent with its distinct FAD-directed covalent mode. Collectively, these structural data support a dual-mechanism for TAS1440—inhibition of LSD1 demethylase activity and disruption of the INSM1–LSD1 complex—and, together with our modeling (Fig. 5h), are consistent with potential interference at SMAD2-interacting surfaces.

Coordinated Mechanisms of TAS1440 via INSM1-LSD1 Complex-Mediated Transcription and Epigenetic Networks

Focusing on the histone demethylase function and epigenetic regulation of LSD1, we performed ChIP-seq analysis of histone modifications in NCI-H1417 and NCI-H146 cells to identify

transcription factors (TFs) involved in TAS1440-mediated epigenetic reprogramming. TAS1440 markedly increased genome-wide metaprofiles of H3K4me1, H3K4me2, and H3K27ac compared to the DMSO control (Fig. 6a and Supplementary Fig. 11h). In contrast, H3K4me3 levels remained unchanged or were slightly reduced, likely reflecting LSD1's substrate specificity and preference for H3K4me1 and H3K4me2 over H3K4me3, as previously reported[22].

Similar effects on histone modifications were observed with ORY-1001 and GSK2879552. However, TAS1440 produced markedly larger increases in H3K4me1 and H3K4me2 meta-signals (Fig. 6a and Supplementary Fig. 11h). By contrast, ORY-1001 and GSK2879552 caused a more substantial reduction in H3K4me3 levels than TAS1440; the basis for this difference remains to be clarified. Overall, these data indicate global epigenetic reprogramming consistent with LSD1 catalytic inhibition and emphasize TAS1440's capacity to modulate histone methylation, acetylation, and downstream transcription in SCLC-A.

Motif analysis of regions with increased H3K4me2 identified 247 enriched motifs in NCI-H1417 and 226 enriched motifs in NCI-H146 (Fig. 6b and Supplementary Fig. 11i). Analogous analyses for H3K4me1 and H3K27ac yielded overlapping motif sets in both cell lines. Notably, four motifs consistently enriched across all three sets corresponded to the transcription factors INSM1, SMAD2, SP4, and YY1 in NCI-H1417 and three motifs—INSM1, SMAD2, and SP4—in NCI-H146 (Fig. 6b, c and Supplementary Fig. 11i, j). These transcription factors dissociated from the LSD1 complex upon TAS1440 treatment, indicating their pivotal role at the intersection of LSD1 demethylase-dependent epigenetic regulation and transcription factor activation following LSD1 repressor-complex disruption. Accordingly, we conducted further analyses to elucidate the roles of these transcription factors and their interactions with downstream signaling pathways in the context of antitumor responses.

Network mapping revealed candidate LSD1–TFs complex binding sites near the transcription start sites (TSSs) of genes involved in the NOTCH and TGF-β pathways (Fig. 6d and Supplementary Fig. 11k). Specifically, potential LSD1–TFs complex binding sites were detected for these target genes in NCI-H1417 cells: 33 sites for INSM1, 26 for SMAD2, 35 for SP4, and 9 for YY1. For example, we identified several potential INSM1 binding sites near the TSSs of *NOTCH1* and *NOTCH3*, and these sites became more accessible, as indicated by increased H3K4me2 and, at selected loci, H3K4me1 and H3K27ac after LSD1 inhibitor treatment (Fig. 6e, f and Supplementary Fig. 11a, b). Similarly, potential INSM1 binding sites were identified near the TSS of the *TGFB2* gene, which also transitioned to an epigenetically active state after treatment with LSD1 inhibitors (Supplementary Fig. 11d, e). Similar results were observed in NCI-H146 cells, confirming that these effects are not cell line-specific (Supplementary Fig. 11l–o).

These results were further supported by INSM1- and SMAD2-ChIP assays. INSM1-ChIP showed that TAS1440 increased INSM1 binding near the TSSs of *NOTCH1* (TSS1, −458 bp; TSS2, +482 bp), *NOTCH3* (TSS2, +588 bp), and *TGFB2* (+470 bp) and, compared with other LSD1 inhibitors, produced stronger enrichment at these promoter-proximal sites except at *NOTCH3* TSS1 (−533 bp) (Fig. 6g and Supplementary Fig. 11c, f). SMAD2-ChIP likewise confirmed increased SMAD2 occupancy near the *NOTCH1* (TSS1, −458 bp; TSS2, +482 bp) and *TGFB2* (+470 bp) promoters, again exceeding the enrichment observed with other LSD1 inhibitors (Fig. 6h and Supplementary Fig. 11g). These findings support a model in which TAS1440 coordinates activation of NOTCH and TGF-β signaling by combining catalytic inhibition of LSD1 with disruption of INSM1–LSD1 and SMAD2–LSD1 corepressor complexes.

Collectively, these findings suggest the potential of TAS1440 as a therapeutic strategy for SCLC-A by targeting INSM1–LSD1 complex-mediated transcriptional and epigenetic networks; by inducing global epigenetic reprogramming together with de-repression of key TFs, TAS1440 preferentially activates tumor-suppressive pathways, including NOTCH and TGF-β.

LSD1 Catalytic Activity is Required for TAS1440-Mediated Effects

LSD1 promotes oncogenesis through its demethylation activity and non-enzymatic scaffolding functions. To dissect the contribution of enzymatic activity to TAS1440's mechanism, we generated a catalytically impaired LSD1 mutant (LSD1-K661A) that hinders demethylase function[9]. Using CRISPR–Cas9, we first knocked out endogenous LSD1 (LSD1-KO) in NCI-H1417 and NCI-H146 cells. These LSD1-KO cells were then reconstituted with 3×FLAG–Myc–LSD1-WT, LSD1-K661A, or empty vector (Fig. 7a, b, d and Supplementary Fig. 12a, b, d). Immunoblotting confirmed loss of H3K4me1/2 demethylase activity in LSD1-K661A (Fig. 7d and Supplementary Fig. 12d; compare lane 4 vs. lane 5).

Comparison of the dose–response curves showed that TAS1440 suppresses growth within the tested concentration range (100–3,000 nM) in parental cells (WT) with endogenous LSD1 (red), whereas LSD1-KO cells (black) remained largely refractory, indicating that TAS1440's antiproliferative activity is LSD1-dependent (Fig. 7c and Supplementary Fig. 12c). To further assess target selectivity, we tested SP2509, a known LSD1 inhibitor with reported off-target activity[23]. Unlike TAS1440, SP2509 retained partial growth inhibition in LSD1-KO cells (green), indicating both LSD1-dependent and -independent actions (Fig. 7c and Supplementary Fig. 12c).

Functionally, both LSD1-WT and LSD1-K661A considerably rescued proliferation in LSD1-KO cells under vehicle (DMSO) (Fig. 7e, f and Supplementary Fig. 12e, f), although LSD1-K661A was less effective. TAS1440 inhibited cell growth in both reconstituted lines, suggesting that enzymatic inhibition contributes to, but does not fully account for, growth effects. At the pathway level, disruption of the LSD1 corepressor complex by KO produced a mild basal induction of NOTCH1 and pSMAD2 (Fig. 7g, lane 2). This increase was completely reversed by LSD1-WT (lane 3) and only partially reversed by LSD1-K661A (lane 4). Upon comparing TAS1440 responses across genotypes, TAS1440 induced NOTCH1 and pSMAD2 in both reconstituted lines (Fig. 7g); however, relative to the parental cells (gray), responsiveness (fold change; TAS1440 vs DMSO) was abolished in LSD1-KO (Empty; yellow), fully restored by LSD1-WT (blue), and not restored by LSD1-K661A (magenta) (Fig. 7h). Consistently, RT-qPCR analysis confirmed reduced activation of NOTCH and TGF-β programs in K661A (Fig. 7i).

RNA-seq showed that TAS1440 had little to no impact on DEGs in LSD1-KO (Empty) cells, consistent with on-target specificity (Fig. 7k, l). By contrast, DEG counts were markedly lower in LSD1-K661A than in LSD1-WT (Fig. 7j, k), and LSD1-WT exhibited the broadest transcriptional response (Fig. 7k, l). KEGG/GSEA showed NOTCH and TGF-β pathway enrichment predominantly in LSD1-WT, attenuated in LSD1-K661A (Fig. 7m). Finally, co-immunoprecipitation showed that TAS1440 disrupts INSM1/SMAD2–LSD1 complexes regardless of catalytic status (Fig. 7n), supporting a dual mechanism of TAS1440—direct inhibition of LSD1 demethylase activity plus co-repressor complex disassembly.

INSM1 Depletion Abrogates TAS1440-Mediated Transcriptional Regulation in SCLC-A and Highlights Its Role in Drug Resistance

To evaluate the requirement of INSM1 for the antitumor effects of TAS1440, we generated INSM1-knockout SCLC-A cell lines using the CRISPR/Cas9 system (Fig. 8a). NCI-H1417 and NCI-H146 cells were electroporated with Cas9/sgRNA complexes targeting *INSM1*, followed by FACS sorting and validation of INSM1 depletion at days 0 and 10. Immunoblotting confirmed loss of INSM1 protein expression (Fig. 8b and Supplementary Fig. 13a), and RT-qPCR corroborated mRNA depletion (Fig. 8c).

We then assessed the impact of INSM1 loss on TAS1440 sensitivity using real-time live-cell imaging (IncuCyte® SX5). TAS1440 robustly inhibited growth in wild-type (INSM1-proficient) cells, whereas this effect was strongly attenuated in INSM1-knockout cells (Fig. 8d and Supplementary Fig. 13b), indicating that INSM1 contributes to the growth-suppressive effects of TAS1440 in SCLC-A.

To elucidate the molecular basis of this drug resistance, we profiled TAS1440-induced gene expression. In wild-type cells, TAS1440 upregulated tumor-suppressive genes in the NOTCH/TGF-β targets (*NOTCH1*, *HES1*, *TGFBR2*, *TGFB2*, and *ID3*), whereas these responses were markedly blunted in INSM1-deficient cells (Fig. 8e and Supplementary Fig. 13c). Furthermore, TAS1440-dependent suppression of *ASCL1* expression, observed in wild-type cells, was also impaired in INSM1-knockout NCI-H1417 cells, suggesting that INSM1 is required for TAS1440-induced repression of neuroendocrine identity. Overall, TAS1440-induced gene expression changes in these pathways were markedly attenuated in INSM1-knockout cells compared to wild-type cells (Fig. 8e and Supplementary Fig. 13c).

RNA-seq identified 1,588 DEGs in TAS1440-treated wild-type versus 234 DEGs in INSM1-knockout cells (Fig. 8f, g, Supplementary Fig. 14a), with NOTCH/TGF-β enrichment primarily in wild-type (Fig. 8h); NCI-H146 showed similar patterns (799 vs. 161 DEGs; Supplementary Fig. 13d–f, Supplementary Fig. 15a). Nevertheless, pathway analysis revealed enrichment of TGF-β and NOTCH signaling upon TAS1440 treatment in both WT and INSM1-knockout cells across NCI-H1417 and NCI-H146 cell lines (Supplementary Fig. 14b and Supplementary Fig. 15b). Interestingly, even in the absence of TAS1440, INSM1-knockout cells displayed upregulation of several TGF-β and NOTCH target genes, such as *NOTCH1* (Supplementary Fig. 14c, e; Supplementary Fig. 15c), consistent with derepression of INSM1-repressed targets. However, TAS1440 failed to further enhance the expression of these genes, suggesting that INSM1 is necessary for dynamic transcriptional reprogramming in response to LSD1 inhibition, rather than maintaining static expression levels.

To determine whether transcription factor activation was also disrupted, we assessed nuclear accumulation of phospho-SMAD2 and NICD. Immunocytochemistry revealed that TAS1440-induced nuclear accumulation of both factors was evident in wild-type cells but absent in INSM1-knockout cells (Fig. 8i, j and Supplementary Fig. 16a, b). These results were supported by immunoblotting (Supplementary Fig. 14d, e), reinforcing the idea that INSM1 loss impairs signal transduction downstream of LSD1 inhibition by TAS1440.

To confirm the functional role of INSM1, we reintroduced INSM1 into the knockout cells (Fig. 8k and Supplementary Fig. 13g). Restoration of INSM1 expression rescued TAS1440 sensitivity in both NCI-H1417 and NCI-H146 cells, as measured by cell viability assays (Fig. 8l; Supplementary Fig. 13h), and reinstated the expression of NOTCH and TGF-β downstream targets, including *NOTCH1, HES1*, and *TGFB2* (Fig. 8m and Supplementary Fig. 13i). Conversely, combination of

INSM1-knockout with SMAD2 knockdown markedly abrogated TAS1440-induced growth suppression and transcriptional changes (Fig. 8l, m and Supplementary Fig. 13g–i), highlighting their cooperative role in mediating TAS1440 sensitivity.

To further dissect the apparent dual role of INSM1 in regulating *NOTCH1* expression, we investigated chromatin-level changes associated with INSM1 loss using ChIP-seq for histone modifications. Given that INSM1 knockdown reduces TAS1440 sensitivity in SCLC-A cells (Supplementary Fig. 13j, k), we next investigated its impact on histone modifications. Consistent with its lack of intrinsic demethylase activity, INSM1 knockdown did not alter H3K4me1/2/3 levels at TSSs (Fig. 8n), indicating that it does not directly regulate methylation. In contrast, we observed a pronounced increase in H3K27ac levels at TSSs in INSM1-knockout cells, suggesting derepression of transcriptional targets. At the gene level, representative tumor-suppressive targets such as *NOTCH1* and *TGFB2* exhibited increased H3K27ac enrichment and transcriptional upregulation in the absence of INSM1 (Fig. 8o–r). These findings support a model in which INSM1 functions as an LSD1-coupled repressor under basal conditions, and its loss both dampens TAS1440-driven dynamic induction and rewires epigenetic states associated with resistance.

INSM1 Overexpression Increases TAS1440 Sensitivity in Non-Neuroendocrine and TAS1440-Resistant Neuroendocrine Cells

To complement our loss-of-function studies, we tested whether gain of INSM1 enhances responsiveness to TAS1440. We ectopically expressed INSM1 in two resistant non-neuroendocrine models—NCI-H211 (SCLC-P) and NCI-H196 (YAP1-high, non-NE)—and confirmed robust protein induction by immunoblotting (Supplementary Fig. 17a). We also

evaluated DMS79 (SCLC-A, neuroendocrine), an intrinsically TAS1440-refractory background, to determine whether enforced INSM1 further increases sensitivity. INSM1 overexpression shifted TAS1440 dose–response curves leftward and increased growth suppression in the two non-NE models relative to empty-vector controls; in DMS79, the enhancement was present but more modest (Supplementary Fig. 17b).

In parallel RNA-seq analyses, INSM1 overexpression did not alter baseline expression of the NE marker *ASCL1* or of *YAP1* and *POU2F3* (Supplementary Fig. 17c). Regarding drug responsiveness, INSM1 overexpression increased the number of TAS1440-induced DEGs in the non-neuroendocrine (non-NE) lines NCI-H211 and NCI-H196, as well as in DMS79—which expresses moderate endogenous INSM1—relative to empty-vector controls (Supplementary Fig. 17d and e). KEGG and GSEA further indicated that INSM1 overexpression augmented TAS1440-mediated enrichment of NOTCH and TGF-β signaling in the non-NE models (Supplementary Fig. 17f). Consistent with these transcriptomic findings, immunoblotting showed that ectopic INSM1 enhanced TAS1440-induced increases in pSMAD2 and the induction of NOTCH1, albeit with cell line–dependent variation, in both previously less-responsive cell lines (Supplementary Fig. 17g, h). Examination of downstream pathway activation by heatmap profiling further revealed that, in the insensitive state (empty vector), few genes changed between DMSO and TAS1440, whereas with INSM1 overexpression, both pathways were partially activated following treatment (Supplementary Fig. 17i, j). Although the dominant downstream effectors of NOTCH/TGF-β may vary by cell line, these findings support a link between the INSM1–LSD1 axis and pharmacologic sensitivity.

Collectively, these data support a model in which INSM1 is both a determinant and an amplifier of TAS1440 response—such that INSM1 gain converts resistant non-NE states toward a

drug-responsive, NE-like program and modestly enhances TAS1440 effects even in an NE-positive context.

TAS1440 Inhibits SCLC-A Tumor Growth in Vivo and Demonstrates Prognostic and Therapeutic Relevance of INSM1–LSD1 Axis in SCLC

To evaluate the in vivo efficacy of TAS1440, we tested four SCLC-A xenograft models (NCI-H1417, NCI-H146, NCI-H510A, and COR-L51). TAS1440 significantly reduced tumor growth in all models (dose group: 16.7 or 50 mg/kg/day in NCI-H1417; 50 mg/kg/day in the others) compared with vehicle (Fig. 9a–e, g; Supplementary Fig. 18e, i). In the NCI-1417 model, ORY-1001 also reduced tumor growth at the tested dose (0.01–0.03 mg/kg/day) (Fig. 9a).

Consistent with *in vitro* findings, immunoblotting of xenograft tumors showed NOTCH1 upregulation and increased pSMAD2 after TAS1440 (Fig. 9h,i; Supplementary Fig. 18f, g, j, k). RT-qPCR confirmed induction of NOTCH/TGF-β-pathway genes (*NOTCH1*, *HES1*, *TGFB2*, *TGFBR2*, *ID3*) and reduction of *ASCL1* and *DLL3*, with some markers showing borderline significance (e.g., *TGFBR2* P = 0.06) (Fig. 9j; Supplementary Fig. 18h, l).

To evaluate INSM1 dependence in vivo, INSM1-wild-type (WT) NCI-H146 xenografts were responsive to TAS1440, whereas INSM1-knockout (KO) NCI-H146 xenografts were non-responsive (Fig. 9f), indicating that INSM1 expression confers TAS1440 sensitivity in vivo.

In an orthotopic NCI-H146 lung model, TAS1440 reduced pulmonary tumor burden, as shown by micro-computed tomography (CT) images and volumetric quantification (Fig. 9k).

Body-weight monitoring showed modest decreases in some TAS1440 groups, with no overt loss relative to vehicle throughout the treatment period (Supplementary Fig. 18a–d).

Finally, survival analysis in a public SCLC RNA-seq cohort [24] showed that high KDM1A expression associates with worse overall survival (HR 2.17, P = 0.0082), whereas INSM1 exhibited a non-significant trend; similar non-significant trends were observed within SCLC-A (Fig. 9l, m). These data support the prognostic and therapeutic relevance of the INSM1–LSD1 axis in SCLC.

Discussion

TAS1440, a histone H3-competitive LSD1 inhibitor, reprograms SCLC transcriptional circuits by releasing repression of tumor-suppressive pathways. In neuroendocrine-high models, particularly SCLC-A, TAS1440 dissociated INSM1 and SMAD2 from the LSD1 complex, activated NOTCH and TGF-β signaling, and achieved stronger growth inhibition *in vitro* and greater tumor regression in xenografts than covalent FAD-directed inhibitors. These results highlight INSM1–LSD1 cooperativity as a key determinant of neuroendocrine identity and provide a mechanistic rationale for selectively targeting SCLC-A.

Clinical trials of irreversible LSD1 inhibitors, such as ORY-1001 and GSK2879552, have faced challenges due to unfavorable risk–benefit profiles[25,26]. For instance, GSK2879552 was evaluated in three clinical trials: one focused on SCLC and two on hematological malignancies, but all were terminated due to safety concerns[27,28]. ORY-1001 demonstrated acceptable safety and signs of activity in a phase I study in relapsed/refractory acute myeloid leukemia[29], and a phase IIa study of ORY-1001 with azacitidine is ongoing[14]. These limitations underscore the need for safer and

more effective reversible LSD1 inhibitors. CC-90011, for example, is being evaluated across multiple trials and combination strategies, showing promising results[17,30,31]. Similarly, through its substrate-competitive mechanism, TAS1440 demonstrates potent efficacy and may offer reduced off-target effects, highlighting its potential as a next-generation therapeutic agent for SCLC.

Mechanistically, TAS1440 engages the histone H3-binding pocket of LSD1, thereby disrupting LSD1 repressive complexes with INSM1 and SMAD2. This dissociation reactivates NOTCH signaling and downregulates neuroendocrine markers including ASCL1, consistent with prior findings for T-3775440[32]. Likewise, ORY-1001 reportedly activates NOTCH signaling and suppresses ASCL1 expression in xenograft models[12]. TAS1440 also upregulated TGF-β-related genes, aligning with previous studies showing that LSD1 complexes suppress TGF-β and NOTCH pathways in various cancers. This relationship is supported by mouse models, in which disruption of INSM1 in pancreatic pre-endocrine cells upregulated genes in these pathways[33], and by observations that LSD1 expression negatively correlates with TGFB1 in human breast cancer cell lines[10]. Collectively, these data indicate that TAS1440 exerts antitumor effects by releasing repression of TGF-β and NOTCH signaling.

INSM1 was initially identified as a transcriptional repressor, shown to bind to promoters such as *HES1* to suppress their transcription[34,35]. Consistently, our findings demonstrate that TAS1440 derepressed NOTCH pathway genes, including HES1. INSM1-binding sites were identified at the promoters of *NOTCH1/2/3*, and TAS1440 considerably increased their expression. Notably, deletion of INSM1 abolished TAS1440-induced NOTCH1 upregulation—likely reflecting elevated basal expression in the absence of INSM1 or the loss of INSM1-dependent activation dynamics. INSM1 autoregulation through promoter binding[36], a feedback mechanism that appears disrupted in SCLC, may further contribute to the gene-specific expression dynamics

observed. In parallel, TAS1440's ability to interfere with LSD1–SMAD interactions underscores its role in activating TGF-β signaling and enhancing transcription of SMAD/TGF-β target genes. Pulmonary neuroendocrine cells (PNECs), rare airway epithelial cells associated with the diffuse neuroendocrine system, are considered a potential origin of SCLC due to their similar morphology and neurosecretory granules[37]. The first SCLC mouse model was generated by conditional inactivation of *Rb1* and *Trp53* in adult respiratory epithelial cells, yielding aggressive SCLC-like tumors[38]. Subsequent studies showed that double knockouts of *Rb1* and *Trp53* more effectively induced SCLC in PNECs than in type II alveolar cells, supporting PNECs as the predominant cell of origin[39]. Unlike lung adenocarcinoma, where driver-guided therapies are established, SCLC has historically been treated as a single disease[1]. The recent delineation of four molecular subtypes with distinct susceptibilities emphasizes the need for subtype-specific strategies[40,41]. For example, MYC-driven reprogramming can activate NOTCH and promote transitions from neuroendocrine SCLC-A to non-neuroendocrine subtypes[41], highlighting the dynamic evolution and heterogeneity of SCLC.

Here, we present a detailed analysis of TAS1440, a potent LSD1 inhibitor with notable activity against SCLC-A, characterized by INSM1 and ASCL1 expression. While the precise basis for selective activity in ASCL1-expressing cells remains to be fully defined, our findings indicated that TAS1440 may offer a potential targeted approach for SCLC-A. Given that SCLC-A accounts for approximately 70% of all SCLC cases[1], TAS1440 could represent an option to address this unmet medical need. Future studies should extend evaluation to other subtypes and test combination strategies, such as immune checkpoint blockade, to maximize therapeutic impact. Limitations of this study include the reliance on subcutaneous xenograft models; orthotopic, syngeneic, and ultimately clinical studies will be necessary to fully assess efficacy. In addition,

body-weight loss observed in TAS1440-treated mice indicated systemic toxicity in preclinical models. Comprehensive toxicological assessments, including hematologic profiling, have been conducted, and a phase 1 clinical trial (NCT04282668) has been completed to further investigate safety and efficacy, although detailed toxicity data are currently under evaluation. These results provide important insights and support continued assessment of the clinical utility of TAS1440.

Acknowledgments

This study was funded by Taiho Pharmaceutical Co., Ltd., Japan, and was supported by Grants-in-Aid for Scientific Research KAKENHI, Scientific Research (B) Cat. No. 19H03708, (C) Cat. No. 20K08397, (B) Cat. No. 21H02974, (Pioneering) Cat. No. 23K17429, (C) Cat. No. 19K07635, and (C) Cat. No. 18K07439. This work was partly supported by the Takeda Science Foundation, the Naito Foundation, the Novartis Foundation (Japan), the Cell Science Research Foundation, the Princess Takamatsu Cancer Research Fund, the Ichiro Kanehara Foundation for the Promotion of Medical Sciences and Medical Care, the Hamaguchi Biochemistry Foundation, the Mochida Memorial Foundation for Medical and Pharmaceutical Research, the Yamaguchi Endocrine Foundation, and the Donated Fund of Next Generation Hormone Academy for Human Health & Longevity.

Author Contributions

T.Ma. conceived the study. T.T. contributed to the conceptualization and study design, developed the methodology, acquired funding, and provided project administration and resources. S.O. provided project administration and resources, supervised the study, and reviewed and edited the

manuscript. T.Ma., Y.G., S.T., A.O., A.N., N.H., T.O., T.Mi., S.Y., T.S., R.H. and Y.Ko. analyzed and interpreted the data. Y.Ka. and O.O. performed the proteomic analyses. T.S. contributed to methodology and data visualization. Y.G. performed the animal, cell-based, protein and RNA experiments. S.T., H.Y. and M.C. performed cell-based experiments. T.F. performed cell immunostaining and animal experiments. A.N., R.K., Y.U., H.S., M.Y. and I.S. performed animal experiments. M.N. generated the plasmid constructs. S.Y., T.S., R.H. and Y.Ko. performed additional investigations. T.Ma., S.T., A.N., N.H., T.F., Y.T., T.K., S.Y. and Y.Ko. validated the findings. T.Ma., Y.G., S.T., A.O., A.N., N.H., T.S., R.H. and Y.Ko. prepared the figures and visualized the data. T.Ma., Y.G., A.O., N.H. and T.F. drafted the manuscript. Y.G., A.O., N.H., R.K. and S.M. reviewed and edited the manuscript. All authors approved the final manuscript.

Competing Interest

None of the authors affiliated with Chiba University (Yingbo Gong, Atsushi Onodera, Akitoshi Nakayama, Naoko Hashimoto, Takahiro Fuchigami, Motoi Nishimura, Tomohiro Ogino, Ryota Kurimoto, Yasufumi Uematsu, Hidemi Suzuki, Hongye Yu, Mingyang Chen, Masataka Yokoyama, Ikki Sakuma, Yuki Taki, Takashi Kono, Takashi Miki, Shinichiro Motohashi, and Tomoaki Tanaka) have any competing interests. None of the authors affiliated with Kazusa DNA Research Institute (Yusuke Kawashima and Osamu Ohara) have any competing interests. Takumitsu Machida, Sayaka Tsukioka, Satoshi Yamashita, Tatsuya Suzuki, Ryo Hatanaka, Yasuo Kodama, and Shuichi Ohkubo are full-time employees of Taiho Pharmaceutical Co., Ltd.

Figure legends

Figure 1: Transcriptome-based classification of 22 small-cell lung cancer (SCLC) cell lines into four molecular subtypes.

(a) Study workflow. RNA-seq was performed for 22 SCLC cell lines (n = 3 independent biological samples per line). Cell lines were assigned to one of four subtypes—SCLC-N, SCLC-Y, SCLC-A, and SCLC-P—according to the dominant expression of the defining transcription factor (NEUROD1, YAP1, ASCL1, and POU2F3, respectively). Nineteen lines were subsequently used for analyses of response to LSD1 inhibitors (not shown).

(b) Correlation matrix for all 22 SCLC cell lines. Pairwise Pearson correlation coefficients (PCCs) among the 22 lines based on RNA-seq expression profiles (triplicates per line); colors denote the strength and sign of the correlation.

(c) Defining transcription factors. Heatmap of NEUROD1, YAP1, ASCL1, and POU2F3 across the 22 lines. Values are row-wise Z-scores (scale −4 to +4); columns are ordered by subtype assignment.

(d) Subtype-signature genes. RNA-seq heatmap showing expression patterns of curated signature genes across the four subtypes. Rows represent genes, and columns represent cell lines (ordered as in c); values are row-wise Z-scores (triplicates per line).

(e) Examples of differentially expressed genes. Box-and-whisker plots illustrating subtype-specific expression of NEUROD1, YAP1, ASCL1, POU2F3, INSM1, SMARCA4, SYK, ETS2, DLL3, and CRACDL. Boxes summarize line-level mean FPKM values within each subtype (per-line mean from n = 3 independent biological samples). Significance was assessed by one-way ANOVA across subtypes (****P < 0.0001; ***P < 0.001; **P < 0.01; *P < 0.05). Data are presented as box-and-whisker plots where the center line represents the median, box limits represent the upper and lower quartiles, and whiskers represent the minimum and maximum values.

Source data are provided as a Source Data file. See also Supplementary Fig. 1. Abbreviations: SCLC, small-cell lung cancer; PCC, Pearson correlation coefficient; FPKM, fragments per kilobase of transcript per million mapped reads.

Figure 2: TAS1440 demonstrates subtype-selective growth suppression in SCLC-A and high biochemical selectivity for LSD1.

(a) Effects of TAS1440, ORY-1001, and GSK2879552 on three SCLC subtypes (SCLC-N, SCLC-A, SCLC-P). Data are shown as box-and-whisker plots (min to max) across cell lines in each subtype; each cell line was assayed in triplicate (n = 3 independent biological samples). Cell growth was normalized to the DMSO control on day 8 using: Cell growth (%) = (A/B) × 100, where A = cell number in the treated group on day 8 and B = cell number in the control group on day 8. Statistical significance was determined by one-way ANOVA (two-sided): *P < 0.05; N.S., not significant.

(b) Within-subtype comparison among inhibitors. Effects of 8 days of treatment on three distinct SCLC subtypes with three LSD1 inhibitors (TAS1440, ORY-1001, and GSK2879552 at 7,500 nM); experiments were performed in triplicate for each cell line (n = 3 independent biological samples). Data are presented as box plots (min-max). ***P < 0.001, **P < 0.01, N.S., not significant, as determined by one-way ANOVA (two-sided).

(c) Dose-response curves (0–7,500 nM). Growth inhibition in the indicated cell lines following treatment with TAS1440 (red), GSK2879552 (green), or ORY-1001 (blue). The mean ± SEM of triplicate samples (n = 3 independent biological samples) are shown (****P < 0.0001, ***P < 0.001, **P < 0.01; N.S. not significant, two-sided one-way ANOVA).

(d) Potency summary. IC_{50} values for TAS1440 (red), ORY-1001 (blue), and GSK2879552

(green) across 19 SCLC cell lines. Bars at ">7,500 nM" indicate no detectable inhibition at the highest concentration tested. The IC_{50} values were determined using TAS1440 and ORY-1001 at 10 different concentrations. See also Supplementary Fig. 2.

(e) Chemical structure of TAS1440 (benzoate salt).

(f) IC_{50} values of TAS1440 for the inhibition of LSD1, LSD2, MAO-A, and MAO-B were calculated to determine the selectivity of TAS1440 (n = 2 independent experiments).

(g) Histone-substrate competition assay to calculate the IC_{50} values of TAS1440 and ORY-1001 for inhibiting LSD1 in the presence of different concentrations of substrate (histone H3) (n = 2 independent experiments). Abbreviations: SCLC, small-cell lung cancer; LSD1, lysine-specific demethylase 1; LSD2, lysine-specific demethylase 2; MAO-A/B, monoamine oxidase A/B; DMSO, dimethyl sulfoxide; SEM, standard error of the mean. Source data are provided as a Source Data file.

Figure 3: TAS1440 modulates gene expression programs associated with growth response in SCLC.

(a) Global relationship between drug response and transcriptional change. Bubble plot of 19 SCLC cell lines showing the correlation between the number of upregulated DEGs (y-axis) and cell growth inhibition (%) in different SCLC subtypes after treatment with TAS1440 (300 nM, x-axis). Bubbles are colored by subtype (SCLC-A, SCLC-N, SCLC-P) and scaled to DEG counts (range <30–1,786). "Sensitive" and "Insensitive" groups are separated by the dashed line. Cell growth was calculated as described in Fig. 2 (mean values, n = 3 independent biological samples in each group).

(b) Summary by cell line of response and DEG burden. Concentric ring plot of the 19 cell lines

showing, from inner to outer rings: subtype, numbers of TAS1440-induced DEGs (≥2-fold vs. DMSO; upregulated = green, downregulated = yellow); and cell growth at day 8 (% of DMSO; values on the rim). SCLC-A lines cluster with greater growth reduction and larger DEG burdens (upregulated ≈30–1,786 across lines).

(c) Baseline KDM1A expression and drug sensitivity. Box-and-whisker plots (min-max) comparing KDM1A (FPKM) between sensitive and insensitive groups in all 19 SCLC lines (left) and in the 12 SCLC-A lines (right). Center line represents the median, box limits represent the upper and lower quartiles, and whiskers represent the minimum and maximum values. **$P < 0.01$, *$P < 0.05$ by two-sided Student's t-test ($n = 3$ independent biological samples per cell line).

(d) NOTCH pathway activity and drug sensitivity. Box-and-whisker plots (min-max) of normalized enrichment scores (NES) for the NOTCH signaling pathway in sensitive vs. insensitive groups for all 19 lines (left) and the 12 SCLC-A lines (right). Center line represents the median, box limits represent the upper and lower quartiles, and whiskers represent the minimum and maximum values. *$P < 0.05$ by two-sided Student's t-test ($n = 3$ independent biological samples per cell line).

(e) Gene-level association analysis across lines. For each gene, the Pearson correlation coefficient (PCC) between TAS1440-induced log2 fold-change and cell growth (%) was computed across all 19 lines. Genes with $|PCC| \geq 0.5$ were selected. The heatmap displays PCCs (first column) and per-line log2 fold-changes (remaining columns), ordered by subtype; the bar plot below shows the growth (%) for each line. Representative positively associated genes include TGF-β-related factors (e.g., SMAD6, BMP5, FBN1, TGFB2), while negatively associated genes include SCLC-A markers (e.g., ASCL1, INSM1) and DLL3. Cell growth (%) was calculated as in Fig. 2.

(f) Examples of gene-response correlations. Scatter plots for selected genes illustrate the

correlation between log2 fold-change and growth (%) after TAS1440 across subtypes, with Pearson's r and P values shown. Points are colored by subtype. Abbreviations: SCLC, small-cell lung cancer; DEG, differentially expressed gene; DMSO, dimethyl sulfoxide; NES, normalized enrichment score; PCC, Pearson correlation coefficient; FPKM, fragments per kilobase of transcript per million mapped reads. Source data are provided as a Source Data file.

Figure 4: TAS1440-driven temporal dynamics of gene expression and TGF-β/NOTCH pathway activation in SCLC-A.

(a) Time-course RNA-seq in NCI-H1417. Heatmap showing gene-wise Z-scored expression across Days 0, 1, 2, 3, 5, and 7 after TAS1440 treatment (300 nM unless indicated; n = 3 independent biological samples per time point, DMSO controls matched). Genes belonging to NOTCH or TGF-β signaling are annotated.

(b) Pathway enrichment over time. KEGG gene set enrichment across days (upper heatmap) and GSEA enrichment plots at Day 5 (lower panels). NOTCH and TGF-β signaling are positively enriched at Day 5 (NES = 1.46 and 1.33, respectively; $P < 0.001$).

(c) Early and delayed signaling kinetics by immunoblot. Cells were treated with TAS1440 (300 nM). pSMAD2 increased rapidly, peaking at 30–45 min (~2.3-fold vs. 0 h) and falling below baseline by 2–24 h, while total SMAD2 was unchanged. In a separate time course, NOTCH1 accumulated more slowly, reaching a maximum at days 3–4 (~25-fold vs. day 0) and declining by day 7. Band intensities were normalized to GAPDH and expressed relative to the 0-time point for each series. Representative blots from three independent experiments are shown.

(d) Localization of pSMAD2 after TAS1440 treatment for 2 h. Representative immunofluorescence images and quantification of pSMAD2-positive nuclei (%). Scale bars, 10

μm. Data are presented as mean ± SD (n = 7 independent fields); ****P < 0.0001 by two-sided Student's t-test.

(e) Localization of the NOTCH intracellular domain (NICD) after TAS1440 treatment for 3 days. Immunofluorescence of NICD and quantification of NICD-positive nuclei (%). Scale bars, 10 μm. Data are presented as mean ± SD (n = 7 independent fields); ****P < 0.0001 by two-sided Student's t-test.

(f) Summary heatmap showing time-dependent changes in the expression of DEGs associated with NOTCH or TGF-β signaling in NCI-H1417 cells that were treated with TAS1440 (n = 3 independent biological samples in each group).

(g) Functional rescue of growth inhibitory effects. Seven-day growth inhibition by TAS1440 (100–3,000 nM) was attenuated by LY411575 (γ-secretase/NOTCH inhibitor, 1 μM), SB431542 (TGF-β type-I receptor inhibitor, 1 μM), or SMAD2 siRNA; the siSMAD2 + LY411575 combination showed the greatest rescue. Data are presented as mean ± SD (n = 4 independent biological samples). ****P < 0.0001, ***P < 0.001, **P < 0.01, as determined by one-way ANOVA. Growth inhibition (%) is relative to DMSO, as in Fig. 2.

(h) Reversal effect of TAS1440-induced mRNA expression. RT-qPCR of NOTCH1, HES1, TGFB2, and TGFBR2 after 7 days shows TAS1440-induced up-regulation that is reduced by LY411575, siSMAD2, and most strongly their combination. Values are normalized to ACTB and expressed relative to DMSO (mean ± SD, n = 3 independent biological samples; one-way ANOVA; ****P < 0.0001, **P < 0.01; N.S., not significant). The fold changes in expression compared with expression in the DMSO treatment group are shown.

(i) Across-LSD1 inhibitor RNA-seq comparison. Heatmap at Day 5 comparing DMSO with five LSD1 inhibitors—TAS1440, ORY-1001, GSK2879552, CC-90011, and SP2509—in NCI-H1417

(n = 3 independent biological samples per condition). Genes related to NOTCH or TGF-β signaling are annotated; values are gene-wise Z-scores.

(j and k) Early and delayed signaling across inhibitors. Immunoblots after 30 min (j) and 3 days (k) of treatment with the five inhibitors. SMAD2, pSMAD2 (j), and NOTCH1 (k) were quantified by densitometry, normalized to GAPDH, and summarized in right-hand bar charts relative to DMSO (mean ± SD, n = 3 independent experiments; one-way ANOVA; ****P < 0.0001, ***P < 0.001, **P < 0.01, *P < 0.05). For example, at 30 min, pSMAD2 increased by approximately 2.9-fold with TAS1440 but only minimally with the other inhibitors, whereas at Day 3, NOTCH1 showed the greatest increase with TAS1440 (~25-fold). See also Supplementary Fig. 6. Source data are provided as a Source Data file.

Figure 5: Proteomic mapping of nuclear LSD1 interactors and TAS1440-induced disruption of the INSM1–LSD1 complex in NCI-H1417 cells.

(a) AP-MS workflow. Purification of LSD1 complex and identification of LSD1-interacting proteins. Nuclear extracts from NCI-H1417 cells transiently expressing 3×FLAG-MYC-LSD1 or 3×FLAG-MYC (empty vector) were treated for 2 h with 0.1% DMSO or 300 nM TAS1440, ORY-1001, or GSK2879552, followed by anti-FLAG immunoprecipitation. Pulldowns were resolved by SDS-PAGE, visualized by silver staining, and analyzed by LC-MS/MS.

(b) Interactor counts with and without TAS1440. After removing proteins detected in the empty-vector control, we identified 422 nuclear factors plus 67 epigenetic regulators in DMSO and 498 plus 77, respectively, after TAS1440 (n = 1 experiment).

(c) Classification by inhibitor responsiveness. For each nuclear/epigenetic protein, the log2 fold change of Mascot scores (control/TAS1440) was used to classify LSD1 interactors as dissociated

by TAS1440 (log2 > 2; red), associated by TAS1440 (log2 < −2; blue), or unchanged (−1 ≤ log2 ≤ 1; gray). Dot size reflects the larger Mascot score between conditions. Numbers (nuclear; epigenetic) are: associated 154 (23), unchanged 344 (54), dissociated 78 (13); candidates boxed (e.g., INSM1, HDAC1/2, SMAD2, RCOR1) were validated in (e, f).

(d) Cross-inhibitor comparison of complex dissociation. Scatter plot comparing TAS1440- versus GSK2879552-induced binding changes, shown as log2(DMSO/drug) Mascot scores (x, GSK2879552; y, TAS1440). The upper-right quadrant indicates common dissociation; off-diagonal points indicate inhibitor-selective effects (upper-left, TAS-selective; lower-right, GSK-selective), whereas RCOR1 remains near the origin.

(e) Co-immunoprecipitation (co-IP) validation across five inhibitors. Cells were treated (2 h) with TAS1440, ORY-1001, GSK2879552, CC-90011, or SP2509; FLAG-LSD1 immunoprecipitates were subjected to immunoblotting for INSM1, HDAC1, HDAC2, SMAD2, and RCOR1. Normalized binding relative to DMSO shows marked loss with TAS1440—INSM1 0.24×, HDAC1 0.17×, HDAC2 0.31×, and SMAD2 0.44×—while RCOR1 is largely retained (~1.07×). A representative blot from three independent experiments is shown.

(f) Quantification of binding to FLAG-LSD1. Bar graphs show co-IP signal for INSM1, HDAC1, HDAC2, SMAD2, and RCOR1, normalized to the DMSO control (mean ± SD, n = 3 independent experiments). P values from one-way ANOVA: ****P < 0.0001, ***P < 0.001, **P < 0.01, *P < 0.05.

(g) Docking simulation using AutoDock Vina predicted inhibitor binding within the FAD-containing catalytic pocket of LSD1 (PDB 2HKO) near Lys661, with estimated binding energies (kcal/mol): TAS1440 −10.1, GSK2879552 −9.1, SP2509 −8.9, CC-90011 −8.8, ORY-1001 −7.0.

(h) Structural predictions by AlphaFold3 multimer models predict direct binding interfaces for

LSD1-INSM1 (left) and LSD1-SMAD2 (right).

(i) Structural overlay. Superposition of LSD1 co-crystal structures complexed with TAS1440 (PDB 8JF5, yellow) and GSK2879552 (PDB 6NQU, blue), together with the INSM1 peptide (PDB 3ZMS, pink) and FAD (orange), illustrating the spatial proximity of inhibitor poses to the INSM1-binding path within the catalytic cavity. The LSD1 backbones are shown as white cartoon models, and the FAD cofactors as orange stick models. Abbreviations: AP-MS, affinity purification-mass spectrometry; LC-MS/MS, liquid chromatography-tandem mass spectrometry; FAD, flavin adenine dinucleotide. Source data are provided as a Source Data file.

Figure 6: Epigenetic reprogramming and TGF-β/NOTCH pathway activation driven by TAS1440 via INSM1-LSD1 complex in NCI-H1417 cells.

(a) Meta-profiles and heatmaps of ChIP-seq signal for H3K4me1, H3K4me2, H3K4me3, and H3K27ac centered on transcription start sites (TSS; ±4 kb) following DMSO, TAS1440, ORY-1001, or GSK2879552 treatment. Upper panels show mean normalized read counts; lower panels show corresponding heatmaps (n = 3 independent biological samples per group).

(b) Motif enrichment and proteomics overlap. Differentially methylated regions (DMRs; H3K4me1/2) and differentially acetylated regions (DARs; H3K27ac) induced by TAS1440 were subjected to de novo motif analysis. The Venn diagram summarizes the overlap between predicted TF motifs and TFs detected by LC-MS/MS as dissociating from the LSD1 complex upon inhibitor treatment (see also Fig. 5c).

(c) Representative motif logos for the four TFs enriched across marks in NCI-H1417—INSM1, SMAD2, SP4, and YY1.

(d) Circos plot linking the four TFs in (c) to promoters (±1 kb) of TAS1440-induced DEGs within the NOTCH and TGF-β pathways.

(e) Genome-browser views of the NOTCH1 locus showing ChIP-seq tracks for H3K4me1 (tracks 1 to 4), H3K4me2 (tracks 5 to 8), H3K4me3 (tracks 9 to 12), and H3K27ac (tracks 13 to 16) under each treatment. Putative INSM1- and SMAD2-binding sites and the qPCR amplicons used for ChIP-qPCR are indicated; a magnified region is shown at right.

(f) Quantification of normalized ChIP-seq signal around the NOTCH1 TSS window (chr9: 139,438,062–139,441,862). Bars show mean ± SD (n = 3 independent biological samples); one-way ANOVA with significance denoted as ****P < 0.0001, ***P < 0.001, **P < 0.01, *P < 0.05; "N.S." not significant.

(g) INSM1 ChIP-qPCR at NOTCH1 promoter-proximal sites (TSS1, −458 bp; TSS2, +482 bp) and a negative control region (−7,178 bp). Data are presented as mean ± SD (n = 6 independent biological samples); one-way ANOVA with significance denoted as ****P < 0.0001, ***P < 0.001, **P < 0.01.

(h) SMAD2 ChIP-qPCR at the same NOTCH1 sites (TSS1, −458 bp; TSS2, +482 bp) and negative control. Data are presented as mean ± SD (n = 3 independent biological samples). Source data are provided as a Source Data file.

Figure 7: LSD1 enzymatic activity underlies TAS1440 responses while complex disruption is catalytic-status independent.

(a) Workflow schematic for generating LSD1-knockout (LSD1-KO) NCI-H1417 cells, followed by reconstitution with 3×FLAG-MYC-LSD1-WT, LSD1-K661A (catalytically impaired), or empty vector (EV) and treatment with DMSO or TAS1440.

(b) Immunoblotting analysis confirming loss of endogenous LSD1 in KO cells (GAPDH loading control). Representative blot from three independent experiments.

(c) Dose-response growth curves over 7 days (100–3,000 nM), monitored by IncuCyte®, for TAS1440 and SP2509 in parental (WT) versus LSD1-KO cells; data shown as % of DMSO. LSD1-KO cells are refractory to TAS1440, whereas SP2509 retains partial activity. Statistics at day 7: one-way ANOVA, mean ± SD (n = 4 independent biological samples), ****P < 0.0001.

(d) Reconstitution validation by immunoblotting analysis showing FLAG-tagged LSD1-WT or LSD1-K661A expression in LSD1-KO cells and baseline histone marks (H3K4me1/2/3, H3, H3K27ac). Representative blot from three independent experiments.

(e) Live-cell proliferation time course determined by live-cell imaging using the IncuCyte® system (+ TAS1440 1,000 nM) for EV, LSD1-WT, and LSD1-K661A reconstitutions (n = 4 independent biological samples).

(f) Day-7 cell-number quantification from (e). Bars denote mean ± SD (n = 4 independent biological samples); one-way ANOVA with multiple comparisons: ****P < 0.0001, **P < 0.01, *P < 0.05, N.S. not significant.

(g) Effect of reconstitution on TAS1440-induced signaling. LSD1-KO NCI-H1417 cells were reconstituted with EV, 3×FLAG-MYC-LSD1-WT, or catalytically impaired LSD1-K661A and then treated ± TAS1440 (300 nM). pSMAD2/SMAD2 and NOTCH1 were assayed at 30 min and

3 days, respectively, using immunoblotting. Band intensities were quantified after normalization to GAPDH. FLAG-LSD1 confirms reconstitution. Shown is a representative blot from three independent experiments.

(h) Densitometric quantification across reconstitution groups. Fold change (TAS1440/DMSO) of NOTCH1 (day 3) and pSMAD2 (30 min), normalized to GAPDH, is shown for EV, LSD1-WT, and LSD1-K661A (mean ± SD, n = 3 independent experiments; one-way ANOVA; **P < 0.01, *P < 0.05; “N.S.” not significant).

(i) RT-qPCR (day 7) of NOTCH1, HES1, TGFB2, TGFBR2, ID3, and ASCL1 mRNA expression normalized to ACTB and expressed as fold change vs. DMSO (mean ± SD, n = 3 independent biological samples; ****P < 0.0001, ***P < 0.001, **P < 0.01, *P < 0.05, N.S. not significant, determined using one-way ANOVA).

(j) Bar graph showing the number of differentially expressed genes (DEGs) after TAS1440 treatment in EV-, LSD1-WT-, and LSD1-K661A-reconstituted cells (upregulated, red; downregulated, blue).

(k) MA plots of TAS1440-induced gene-expression changes (TAS1440 vs. DMSO) in LSD1-KO cells reconstituted with Empty (left), LSD1-WT (middle), or LSD1-K661A (right).

(l) RNA-seq heatmap showing global changes in DEGs in LSD1-KO NCI-H1417 cells reconstituted with EV, LSD1-WT, or LSD1-K661A (n = 3 independent biological samples per group) after TAS1440 vs. DMSO treatment. Genes associated with NOTCH and TGF-β signaling are annotated.

(m) KEGG gene-set enrichment analysis (GSEA) summarizing TAS1440-induced pathways across EV, LSD1-WT, and LSD1-K661A reconstitutions; normalized enrichment scores (NES) are shown, indicating dependence on LSD1 catalytic activity.

(n) LSD1-KO NCI-H1417 cells were reconstituted with EV, 3×FLAG-MYC-LSD1-WT, or 3×FLAG-MYC-LSD1-K661A and treated ± TAS1440 (300 nM, 2 h). Co-IP with anti-FLAG followed by immunoblotting was used to assess LSD1-INSM1 and LSD1-SMAD2 interactions. Representative blot from three independent experiments. Source data are provided as a Source Data file.

Figure 8: INSM1 knockout abolishes TAS1440-mediated tumor suppression and transcriptional reprogramming in SCLC-A.

(a) Schematic of CRISPR-Cas9 editing, FACS isolation, and subsequent TAS1440 treatment workflow in NCI-H1417 cells.

(b) Immunoblot confirming loss of INSM1 protein at days 0 and 10. Representative blot from three independent experiments.

(c) INSM1 mRNA expression was examined by RT-qPCR (mean ± SD; n = 5 independent biological samples; ****$P < 0.0001$, two-sided Student's t-test).

(d) Dose-response growth curves (day 10) monitored by IncuCyte®; INSM1-KO NCI-H1417 cells are refractory to TAS1440 relative to WT (mean ± SD; n = 6 independent biological samples; ****$P < 0.0001$ at day 10, determined using two-sided Student's t-test).

(e) RT-qPCR of pathway targets (NOTCH1, HES1, TGFBR2, TGFB2, ID3) and ASCL1; fold change (TAS1440 vs. DMSO) (mean ± SD; n = 5 independent biological samples; ****$P < 0.0001$, **$P < 0.01$, *$P < 0.05$, determined using one-way ANOVA).

(f) MA plots showing TAS1440-induced gene-expression changes in INSM1 WT (left) and KO (right).

(g) The numbers of upregulated (red) or downregulated (blue) genes by TAS1440 in the WT and KO cells are shown.

(h) KEGG/GSEA highlighting TAS1440-induced pathway enrichment of NOTCH and TGF-β signaling in WT but attenuated in INSM1-KO NCI-H1417 cells.

(i) Immunocytochemistry (ICC) for phospho-SMAD2 (pSMAD2) after 2 h ± TAS1440 in WT vs. INSM1-KO NCI-H1417 cells. Scale bars represent 10 μm. The bar graphs show the percentage of cells positive for nuclear pSMAD2. The error bars represent mean ± SD (n = 8 independent fields); ****P < 0.0001, one-way ANOVA, N.S. means “not significant.”

(j) ICC for NOTCH intracellular domain (NICD) after 72 h ± TAS1440; nuclear-positive cell quantification as in (i). Data are presented as mean ± SD (n = 8 independent fields); ****P < 0.0001, one-way ANOVA.

(k) Immunoblotting analysis showed the restoration of INSM1 expression in INSM1-KO cells upon reintroduction of INSM1 or SMAD2 knockdown in INSM1-KO NCI-H1417 cells. Representative blot from three independent experiments.

(l) Rescue assays (Day 7): INSM1 re-expression restored TAS1440 sensitivity, whereas combining INSM1-KO with siSMAD2 further attenuated TAS1440-mediated growth inhibition (mean ± SD; n = 4 independent biological samples; ****P < 0.0001, ***P < 0.001, N.S. not significant, determined using one-way ANOVA).

(m) RT-qPCR (Day 7) of NOTCH/TGF-β pathway targets under rescue (INSM1 re-expression) and co-knockdown (INSM1-KO + siSMAD2); NOTCH1, HES1, TGFBR2, TGFB2, ID3, and ASCL1 are displayed as fold change (TAS1440/DMSO; ACTB-normalized), as in (e) (mean ± SD;

n = 3 independent biological samples; one-way ANOVA; ****P < 0.0001, ***P < 0.001, **P < 0.01, *P < 0.05, N.S., not significant).

(n) Transcription start site (TSS)-centered ChIP-seq metaprofiles (H3K4me1/2/3, H3K27ac) in WT and INSM1-knockdown (INSM1-KD) NCI-H1417 cells ± TAS1440 (mean of n = 3 independent biological samples per group). The x-axis represents the distance from the center of the TSS; the y-axis represents the normalized read count.

(o–r) Genome-browser views at the NOTCH1 (o) and TGFB2 (q) loci with quantification of mark intensities around TSSs (p, r); putative INSM1-binding sites (BS) indicated (mean ± SD; n = 3 independent biological samples; **P < 0.01, *P < 0.05; one-way ANOVA; N.S., not significant). Source data are provided as a Source Data file.

Figure 9: *In vivo* efficacy of TAS1440 in SCLC-A and clinical relevance of the INSM1–LSD1 axis.

(a) Tumor volumes in NCI-H1417 xenografts treated with TAS1440 (16.7 or 50 mg/kg/day) or ORY-1001 (0.01–0.03 mg/kg/day) versus vehicle (n = 5 mice per group; mean ± SEM; ****P < 0.0001, Dunnett's test vs. vehicle; ##P < 0.01, Aspin-Welch t-test for the indicated comparison).

(b–d) Tumor volumes in NCI-H146, NCI-H510A, and COR-L51 xenografts with TAS1440 (50 mg/kg/day) versus vehicle (n = 4–6 mice per group; mean ± SEM; ***P < 0.001, **P < 0.01, *P < 0.05, two-sided Student's t-test at the endpoint).

(e) Box-and-whisker plots (min-max) summarizing endpoint tumor volumes across models/groups (n = 4–6 mice per group; ***P < 0.001, **P < 0.01; N.S., not significant; two-sided Student's t-test). Center line represents the median, box limits represent the upper and lower quartiles, and whiskers represent the minimum and maximum values.

(f) INSM1 dependency in vivo: box-and-whisker plots (min-max) of tumor volumes at day 19 showing that INSM1-wild-type (WT) NCI-H146 xenografts responded to TAS1440 (50 mg/kg/day), whereas INSM1-knockout (KO) xenografts did not (n = 4–5 mice per group; **P < 0.01; N.S., not significant; two-sided Student's t-test). Center line represents the median, box limits represent the upper and lower quartiles, and whiskers represent the minimum and maximum values. (g) Representative images of excised NCI-H146 tumors (vehicle vs. TAS1440).

(h, i) Immunoblotting of xenograft lysates showing induction of NOTCH1 and pSMAD2 after TAS1440; densitometry values normalized to GAPDH are shown below each lane in (h), and bar graphs in (i) summarize vehicle (gray) versus TAS1440 (red) (n = 4–5 independent biological samples; mean ± SD; two-sided Student's t-test at the endpoint: ***P < 0.001, *P < 0.05).

(j) RT-qPCR from excised tumors showing upregulation of NOTCH/TGF-β targets (NOTCH1, HES1, TGFB2, TGFBR2, ID3) and downregulation of ASCL1 (mean ± SD; n = 4–5 independent biological samples; **P < 0.01, *P < 0.05; one-way ANOVA; fold-change vs. vehicle).

(k) Orthotopic NCI-H146 model: representative micro-CT images and quantification of pulmonary tumor area showing a 67% reduction with TAS1440.

(l, m) Kaplan–Meier overall-survival analyses in public SCLC cohorts: high KDM1A associates with worse survival (HR = 2.17, P = 0.0082), whereas INSM1 shows a non-significant trend (l); similar non-significant trends are observed within SCLC-A (m). P-values were calculated using the log-rank test. Source data are provided as a Source Data file.

Methods

Materials Availability

This study did not generate new unique reagents.

Cell Lines and Cell Culture

NCI-H1417 (Cat. No. CRL-5869), NCI-H209 (HTB-172), SHP-77 (CRL-2195), NCI-H211 (CRL-5824), NCI-H196 (CRL-5823), NCI-H146 (HTB-173), NCI-H187 (CRL-5804), NCI-H69 (HTB-119), NCI-H446 [H446] (HTB-171), DMS 79 (CRL-2049), NCI-H510A (HTB-184), DMS 114 (CRL-2066), DMS 53 (CRL-2062), NCI-H2081 (CRL-5920), NCI-H524 [H524] (CRL-5831), NCI-H128 (HTB-120), NCI-H526 (CRL-5811), and NCI-H1694 (CRL-5888) cell lines were purchased from the American Type Culture Collection. Lu-135 (JCRB0170), COR-L51 (92031916), CPC-N (ACC 306), and SBC-5 (JCRB0819) cell lines were obtained from the Japanese Collection of Research Bioresources, the European Collection of Authenticated Cell Cultures, the German Collection of Microorganisms and Cell Cultures GmbH, and the Health Science Research Resources Bank, respectively. All of the above are small-cell lung cancer (SCLC) cell lines and were cultured in medium supplemented with fetal bovine serum (FBS) (Cat#: 10270106, Gibco, Thermo Fisher Scientific). The medium was conditioned in high-glucose RPMI 1640 (Wako, Cat#: 187-02705) with 10% FBS for NCI-H146, NCI-H187, NCI-H69, NCI-H446, NCI-H526, NCI-H524, and DMS 79; in McCoy's 5A (Gibco, Cat#: 16600-082) with 10% FBS for CPC-N; minimum essential medium (Cat#: 21442-25, Nacalai Tesque, Kyoto, Japan) with 10% FBS for SBC-5; F-12K medium (Gibco, Cat#: 11765-054) with 10% FBS for NCI-H510A; Waymouth's medium (Gibco, Cat#: 11220-035) with 10% FBS for DMS 114 and DMS 53; and IMDM medium (Gibco, Cat#: 12440-053) with 20% FBS for NCI-H128 or HITES medium (Gibco, 11330-032) with 10% FBS, insulin (FUJIFILM, Cat#: 093-06351), transferrin (Cat#:

10652202001, Roche Diagnostics, Rotkreuz, Switzerland), hydrocortisone (Cat#: H6909-10ML, Sigma-Aldrich, St. Louis, MO, USA), GlutaMAX (Gibco, Cat#: 35050-061), sodium selenite (FUJIFILM, Cat#: 190-10844), and β-estradiol (Sigma-Aldrich, Cat#: E2758-250MG) for NCI-H2081 and NCI-H1694. Criteria and Rationale for Inclusion or Exclusion of SCLC Cell Lines Used in This Study are provided in Supplementary Table S1.

In Vitro Cytotoxicity Assay

SCLC cell lines were seeded in 96-well plates. The following day, LSD1 inhibitors were serially diluted with DMSO and mixed with culture medium. The mixtures were then added to each well. The final DMSO concentration was 0.075%. Cells were maintained for 8 days with the inhibitors without medium change. Cell viability was assessed using CellTiter-Glo® 2.0 (Promega, Madison, WI, USA).

Cell Proliferation Assay

To analyze cell proliferation after LSD1 inhibition, 5,000 SCLC cells were seeded in 96-well plates and maintained at 37 °C. Live cells were monitored using an IncuCyte® SX5 Live-Cell Imaging and Analysis Instrument (Sartorius, Göttingen, Germany). Cells were labeled with NucLight Rapid NIR Reagent (Cat. No. 4804, Sartorius). IncuCyte® enabled automated counting of monolayer cell cultures.

Chemical Compounds and Antibodies

TAS1440 was designed and synthesized at Taiho Pharmaceutical Co., Ltd. or at Aptuit (Oxford, UK) Ltd. ORY-1001 and GSK2879552 were synthesized by Taiho Pharmaceutical Co., Ltd., and Sanyu Chemical Co., Ltd., respectively. Pulrodemstat (CC-90011) and SP2509 were purchased

from Selleckchem (Houston, TX, USA). LY411575 was purchased from Sigma-Aldrich. SB431542 was purchased from Cayman Chemical Co., Ltd. (Ann Arbor, MI, USA). The anti-GAPDH antibody (Cat. No. GTX100118) was purchased from GeneTex, Inc. (Irvine, CA, USA). Antibodies including anti-FLAG (Cat. No. 14793), anti-LSD1 (Cat. No. 2184), anti-CHD4 (Cat. No. 4245), anti-HDAC1 (Cat. No. 5356), anti-HDAC2 (Cat. No. 57156), anti-SMAD2 (Cat. No. 5339), anti-NOTCH1 (Cat. No. 3608), anti-CoREST (Cat. No. 14567), rabbit anti-mouse IgG (HRP-conjugated, Cat. No. 58802), and mouse anti-rabbit IgG (HRP-conjugated, Cat. No. 93702) were purchased from Cell Signaling Technology (Danvers, MA, USA). Anti-INSM1 (Cat. No. sc-271408) was purchased from Santa Cruz Biotechnology, Inc. (Santa Cruz, CA, USA). Anti-SMAD2 (phospho-Ser467; ab280888) was purchased from Abcam, Ltd. (Waltham, MA, USA). Rabbit anti-mouse immunoglobulins (HRP-conjugated, Cat. No. P0260) were purchased from Agilent (Santa Clara, CA, USA). Donkey anti-rabbit IgG (HRP-conjugated, Cat. No. NA934) was purchased from Cytiva (Marlborough, MA, USA). siRNA oligonucleotides targeting SMAD2 and INSM1 (Cat. No. AM16708) were purchased from Ambion, Thermo Fisher Scientific. NCI-H1417, NCI-H146, or NCI-H510A cells were transfected with siRNAs using Lipofectamine™ RNAiMAX (Thermo Fisher Scientific, Cat. No. 13778150) following the manufacturer's protocol. At 24 h after transfection, reagents were added, and subsequent experiments were performed.

Enzyme Assays

Recombinant human LSD1 (Cat. No. ab80379) and LSD2 (Cat. No. 31479) were purchased from Abcam and Active Motif (Carlsbad, CA, USA), respectively, and used in enzymatic assays. Inhibition of enzymatic activity by TAS1440 was tested using LANCE® time-resolved FRET (TR-FRET). Biotin-H3K4me1 peptide (Cat. No. AS-64355, AnaSpec, Fremont, CA, USA) was

used as a substrate, and its demethylation by LSD1 or LSD2 was detected by the TR-FRET signal generated when a europium-labeled demethylation-site-specific antibody (Eu-labeled anti-H3K4 as energy donor, Cat. No. TRF040-M, PerkinElmer, Shelton, CT, USA) and streptavidin-conjugated Alexa Fluor™ 647 (energy acceptor; Thermo Fisher Scientific, Cat. No. S21374) were in molecular proximity. The substrate concentrations used for substrate-competition assays were 100 nM or 2,000 nM (Fig. 2g) and 200 nM for IC_{50} determination (Fig. 2f). Assays for histone lysine demethylases (JARID1A, JARID1B, UTX, JMJD2B, and JMJD3), histone lysine methyltransferases (SMYD2 and EZH1/EED/SUZ12), histone deacetylase (HDAC1), DNA methyltransferase (DNMT1), and protein arginine N-methyltransferase (PRMT4) were performed by Eurofins Cerep SA (Celle-Lévescault, France). MAO-A and MAO-B assays were performed by Eurofins Panlabs Discovery Services Taiwan, Ltd. (Taipei, Taiwan).

RNA-Seq and Data Analysis

SCLC cell lines were treated for the indicated durations, with different LSD1 inhibitors (TAS1440, 300 nM; ORY-1001, 100 nM; GSK2879552, 3000 nM; CC-90011, 300 nM; SP2509, 300 nM). Total RNA was extracted using TRIzol™ (Invitrogen, Thermo Fisher Scientific). RNA integrity and concentration were measured using a 4200 TapeStation system (Agilent, Santa Clara, CA, USA). RNA-seq libraries were prepared using the NEBNext® Ultra II Directional RNA Library Prep Kit for Illumina (New England Biolabs, Ipswich, MA, USA) with SPRIselect (Cat. No. B23318, Beckman Coulter, Indianapolis, IN, USA) following the manufacturers' protocols. Deep sequencing was performed on an Illumina NovaSeq 6000 (paired-end). Sequenced reads were aligned using Bowtie 2 and TopHat (version 1.3.2), and Cufflinks (version 2.0.2) was used for transcriptome assembly. Gene expression levels were expressed as fragments per kilobase of exon per million mapped reads (FPKM). Differentially expressed genes (DEGs) were identified using

R (version 4.2.0). Heatmaps and dendrograms were generated using R, GraphPad Prism 9.0, or ChiPlot (https://www.chiplot.online/). DEG-related Kyoto Encyclopedia of Genes and Genomes (KEGG) terms were analyzed using gene set enrichment analyses (GSEA; version 4.2.3).

RT–qPCR

Total RNA was extracted using TRIzol™ reagent (Thermo Fisher Scientific). Quantity and purity were evaluated with a NanoDrop spectrophotometer (Thermo Fisher Scientific), and the A260/A280 ratio was used to assess purity. cDNA was synthesized using ReverTra Ace™ qPCR RT Master Mix (TOYOBO, Osaka, Japan). RT–qPCR was performed using Fast SYBR™ Green Master Mix (Thermo Fisher Scientific, Cat. No. 4385614) on a StepOnePlus™ Real-Time PCR System (Thermo Fisher Scientific) using the default fast-mode setting (stage 1: 95.0 °C for 20 s; stage 2: 40 cycles at 95.0 °C for 1 s and 60.0 °C for 20 s). Relative gene expression was quantified using the $2^{-\Delta\Delta Ct}$ method and normalized to AXTB expression. Primers are shown in Supplementary Table S2.

Plasmid Construction

To obtain 3×FLAG-Myc, the myc sequence was seamlessly inserted at the end of the 3×FLAG sequence of p3×FLAG-CMV10 (Cat. No. E7658, Sigma-Aldrich). To generate 3×FLAG-Myc-LSD1, the LSD1 coding sequence from pIDS-LSD1fl (#109157, Addgene, Watertown, MA, USA) was subcloned downstream of the Myc sequence in p3×FLAG-Myc-CMV10 using NEBuilder HiFi DNA Assembly (Cat. No. E5520S, New England Biolabs). Seamless joining was verified by Sanger sequencing. The backbone was then changed to pcDNA3.1+ (V79020, Invitrogen, Thermo Fisher Scientific). pcDNA3-3×FLAG-Myc-LSD1 K661A was generated using NEBuilder HiFi after amplifying fragments harboring the missense

mutation by PCR from the pcDNA3-LSD1 plasmid. pcDNA3-EGFP was a gift from Doug Golenbock (Addgene plasmid #13031). To subclone pcDNA3-GFP-hINSM1 and pLX304-GFP-hINSM1, the coding sequence of human INSM1 was obtained from cDNA and cloned into pcDNA3 with a C-terminal HA tag (pcDNA3-hINSM1-HA). Based on this construct, two GFP-tagged variants were derived: pLX304-hINSM1-GFP, in which the HA tag was replaced with GFP and the sequence cloned into the pLX304 lentiviral vector, and pcDNA3-hINSM1-GFP, in which the GFP-tagged INSM1 sequence was introduced into the pcDNA3 backbone by Gibson Assembly (New England Biolabs). pLenti-PGK-Venus-Fluc (puro) was a gift from Roland Friedel (Addgene plasmid #140328; RRID:Addgene_140328)[42].

LSD1 Immunoprecipitation and LC–MS/MS Analysis

NCI-H1417 cells were electrotransfected with either pcDNA3-3×FLAG-Myc-empty or pcDNA3-3×FLAG-Myc-LSD1. 46 hours later, cells were treated with LSD1 inhibitors for 2 h, harvested, and solubilized in immunoprecipitation buffer: 50 mM Tris-HCl (pH 7.5), 150 mM NaCl, 10% (v/v) glycerol, 0.1% (v/v) Tween-20, 1 mM EDTA, 10 mM NaF, 1 mM DTT, and protease inhibitor cocktail (Cat#: 25955-24, Nacalai Tesque). Cells were lysed on ice for 30 min with gentle shaking and sonicated on a SFX150 Sonifier (Branson, Brookfield, CT, USA) for cycles of 15 s sonication at 50% amplitude followed by 45 s rest. Precipitates were removed by centrifugation at 20,000 × *g* for 10 min at 4 °C, and immunoprecipitation was performed with 50 µL ANTI-FLAG® M2 Affinity Agarose Gel (Cat. No. A2220, Sigma-Aldrich) overnight at 4 °C. After washing with PBS, proteins were eluted with 150 µg/mL 3×FLAG® peptide (Cat. No. F4799, Sigma-Aldrich). Eluates were acetone-precipitated, resuspended in 1× SDS sample buffer, and separated by SDS–PAGE. Gel bands were excised, washed twice with 100 mM ammonium bicarbonate in acetonitrile, and digested with trypsin for 8 h at 37 °C. Peptides (in 0.1% formic

acid) were analyzed by LC–MS/MS using an Advance UHPLC (Bruker, Billerica, MA, USA) and an Orbitrap Velos Pro (Thermo Fisher Scientific). Data were analyzed with Mascot (version 2.5.1, Matrix Science, Boston, MA, USA). A Mascot score >100 indicates that the absolute probability of a random match is $<1 \times 10^{-10}$.

ChIP

NCI-H1417 cells were treated with DMSO or 300 nM TAS1440 for 5 days and cross-linked at 37 °C for 10 min with 1% formaldehyde. Cross-linking was quenched to a final concentration of 125 mM glycine. Cells were lysed in swelling buffer (25 mM HEPES pH 7.9, 1.5 mM $MgCl_2$, 10 mM KCl, and 0.1% (v/v) NP-40) containing protease inhibitors and centrifuged at 5,000 × *g* for 5 min at 4 °C. Nuclei were resuspended in sonication buffer (50 mM HEPES pH 7.9, 140 mM NaCl, 1 mM EDTA, 1% (v/v) Triton X-100, 0.1% (w/v) SDS, and 0.1% (w/v) sodium deoxycholate; ~5×10^6 cells/mL) and sonicated on a Q700 (Qsonica, Newtown, CT, USA) for 20–25 cycles of 15 s on/45 s off at amplitude 60 (total 6,000 J). Insoluble material was removed by two rounds of centrifugation at 16,000 × *g* for 10 min at 4 °C. Supernatants were immunoprecipitated with either IgG (Thermo Fisher Scientific, Cat. No. 10003D), 5 µg SMAD2 antibody (Cell Signaling Technology, Cat. No. 5339) or 5 µg INSM1 antibody (Santa Cruz, Cat. No. sc-271408) prebound to Dynabeads Protein G (Invitrogen) for 24 h at 4 °C, washed, and eluted for 6 h at 65 °C in ChIP elution buffer (50 mM Tris-HCl pH 7.5, 1% (w/v) SDS, 1 mM EDTA). Cross-links were reversed by adding NaCl and RNase A to 160 mM and 20 µg/mL, respectively, and incubating at 65 °C overnight. EDTA was increased to 5 mM, Proteinase K (200 µg/mL) was added, and samples incubated at 45 °C for 2 h. DNA was purified using a Gel/PCR DNA Isolation System (Cat. No.

GP1001, VioGen, Taipei, Taiwan). Samples were analyzed by qPCR at the NOTCH1 promoter (primer sequences in Table S2).

ChIP-Seq and Data Analysis

NCI-H1417 cells were treated with DMSO or 300 nM LSD1 inhibitor (TAS1440, ORY-1001, GSK2879552) for 5 days and processed following the protocol mentioned prior. Libraries were prepared using the NEBNext® Ultra™ II DNA Library Prep Kit for Illumina® (New England Biolabs) with SPRIselect (Cat. No. B23318, Beckman Coulter). Sequencing was performed on an Illumina NovaSeq 6000 (paired-end). Reads were mapped to GRCh37.p13 (hg19) using Bowtie 2. Peaks were called using MACS2 with the broad option; peaks identified in three replicates were used for further analyses. Quantification used the "Annotate Peaks" command in Partek Flow (https://www.partek.com/). Differentially enriched regions (DERs) were detected using the "Gene-Specific Analysis" command in Partek Flow. IGV (Integrative Genomics Viewer) was used for visualization.

Western Blotting

Cells were washed with chilled PBS and lysed in RIPA buffer (25 mM Tris-HCl, pH 7.4; 150 mM NaCl; 1% (v/v) NP-40; 1 mM EDTA; 5% (v/v) glycerol) supplemented with protease and phosphatase inhibitors. Proteins were separated by SDS–PAGE and electrotransferred onto PVDF membranes (Mini-PROTEAN® Tetra system, Bio-Rad, Hercules, CA, USA). Membranes were blocked with 10% (w/v) skim milk followed by 1% (w/v) BSA at 23 °C for 1 h, probed with primary antibodies at 4 °C overnight, washed three times with TBS-T, and incubated with secondary antibodies (Cat. No. NA934, Cytiva; Cat. No. P0260, Agilent) for 1 h at 23 °C. Signals

were visualized using enhanced chemiluminescence (Cytiva, Cat. No. RPN2232) and captured with Fusion FX (Vilber Lourmat, Marne-la-Vallée, France).

For Fig. 4c, anti-GAPDH (Cat. No. GTX100118; 1:5000, GeneTex), anti-SMAD2 (phospho-Ser467, ab280888; 1:1000, Abcam), and anti-NOTCH1 (Cat. No. 3608; 1:1000, Cell Signaling Technology) were used. For Fig. 5e, anti-FLAG (Cat. No. 14793; 1:1000), anti-LSD1 (Cat. No. 2184; 1:1000), anti-HDAC1 (Cat. No. 5356; 1:1000), anti-HDAC2 (Cat. No. 57156; 1:1000), anti-SMAD2 (Cat. No. 5339; 1:1000), and anti-CoREST (Cat. No. 14567; 1:1000) were obtained from Cell Signaling Technology, whereas anti-INSM1 (Cat. No. sc-271408; 1:1000) was obtained from Santa Cruz Biotechnology.

Expression and Purification of LSD1–CoREST

An N-terminal His6 tag, SUMOstar tag, and TEV protease cleavage site fused to LSD1 (residues S172–M833), and its cofactor CoREST (residues R311–E443), were subcloned into MCS1 and MCS2 of pETDuet-1. E. coli BL21 (DE3) CodonPlus cells were transformed and cultured in TB medium containing 50 µg/mL ampicillin at 37 °C to OD600 = 0.6. Expression was induced with 0.1 mM IPTG and continued at 16 °C overnight. Cells were lysed in Buffer A (50 mM Tris-HCl pH 7.5, 300 mM NaCl, 10% (v/v) glycerol, 0.1 mM TCEP), sonicated, and clarified by centrifugation at 16,000 × *g* for 30 min. The supernatant was applied to a HiTrap TALON column equilibrated with Buffer A and eluted with ~50 mM imidazole. Excess FAD was added to the fraction. The N-terminal tag was removed using His6-tagged TEV protease during dialysis in Buffer A for 40 h. The dialysate was applied to a second TALON column to remove the cleaved tag and TEV protease; the flow-through was collected and further purified on a HiLoad 26/600 Superdex 200 pg column equilibrated with 25 mM potassium phosphate (pH 7.2) containing 5%

(v/v) glycerol. The LSD1–CoREST complex was concentrated to 18 mg/mL for crystallization (Bradford method).

Structure Analysis of TAS1440-bound LSD1–CoREST

LSD1–CoREST was initially crystallized by hanging-drop vapor diffusion; small seed crystals (50–200 μm) were obtained from a precipitant containing 50–100 mM N-(2-acetamido)iminodiacetic acid (ADA), pH 6.5, and 1.18–1.28 M sodium potassium tartrate. Larger soakable crystals (200–400 μm) were obtained by macroseeding from a precipitant containing 100 mM ADA (pH 6.5) and 1.22 M sodium potassium tartrate. Crystals were soaked in 100 mM ADA (pH 6.5), 1.22 M sodium potassium tartrate, 10% (v/v) glycerol, and 2 mM TAS1440 at 20 °C for 2 h. Diffraction data were collected at KEK Photon Factory BL-1A and processed using iMOSFLM in the CCP4 suite. The space group was I222. The structure of TAS1440-bound LSD1–CoREST was solved by molecular replacement with MOLREP (CCP4) using PDB 5YJB as a search model and refined with REFMAC5. Manual rebuilding and map interpretation were performed in Coot. Final R-values were R_work = 19.3% and R_free = 23.0%. Coordinates were deposited in the PDB under 8JF5 (statistics in Supplementary Table S3).

Immunofluorescence Analysis

NCI-H1417 or NCI-H146 cells were cultured in 4-well chamber slides (2×10^4 cells per well) and treated with 0.1% (v/v) DMSO or 300 nM TAS1440 for the indicated times. Cells were fixed with 4% paraformaldehyde in PBS for 20 min, permeabilized with 0.1% (v/v) Triton X-100 in PBS for 5 min at 23 °C and blocked with 3% (v/v) FBS in PBS for 60 min. Primary antibodies encompassed cleaved NOTCH1 (Val1744; 1:100, Cell Signaling, Cat. No. 4147S), SMAD2 (1:200, Cell Signaling, Cat. No. 5339S), and INSM1 (1:100, Santa Cruz, Cat. No. sc-271408). Secondary

antibodies were donkey anti-mouse IgG Alexa Fluor™ 488 (1:500, Invitrogen, Cat. No. A32766), donkey anti-mouse IgG Alexa Fluor™ 647 (1:500, Invitrogen, Cat. No. A32787), and donkey anti-rabbit IgG Alexa Fluor™ 594 (1:500, Invitrogen, Cat. No. A32754). Primary incubations were performed at 4 °C overnight, whereas secondary incubations at room temperature for 2 h. Nuclei were stained with DAPI (1 μg/mL; Cat. No. H-1200, Vector Laboratories, Newark, CA, USA). Images were acquired on a Zeiss LSM 980 confocal microscope (Axio Observer 7; 20× Plan-Apochromat or 63× Plan-Apochromat Oil) and analyzed using ZEN Blue v3.2. Nuclear phospho-SMAD2- and NICD-positive cells were quantified on a BZ-X800 fluorescence microscope (KEYENCE, Osaka, Japan) equipped with the BZ-H4C image cytometer module.

INSM1-KO or LSD1-KO NCI-H1417 and NCI-H146 Cells

The CRISPR/Cas9 system was employed as previously described [35,42]. The backbone vector pSpCas9(BB)-2A-GFP (PX458) was obtained from Addgene. The gRNA sequence targeting INSM1 was 5′ -CTCGCCGCCGCGGACCCGGT-3′ , and that targeting LSD1 was 5′ -CCGGCCCTACTGTCGTGCCT-3′ . Oligos were annealed and phosphorylated using T4 DNA Ligase Reaction Buffer and T4 Polynucleotide Kinase (New England Biolabs) at 37 °C for 30 min and 95 °C for 5 min, respectively. PX458 was digested with BbsI (Thermo Fisher Scientific) at 37 °C for 30 min and purified using a QIAquick Gel Extraction Kit (QIAGEN). PX458 and the annealed oligos were ligated at room temperature for 10 min using a Quick Ligation Kit (New England Biolabs) and treated with PlasmidSafe™ exonuclease (Cambio, Cambridge, UK) at 37 °C for 30 min. Plasmids were transformed into One Shot™ Stbl3™ chemically competent *E. coli*, and amplified plasmids purified with NucleoBond Xtra Midi (Takara Bio, Shiga, Japan). The INSM1 or LSD1 CRISPR/Cas9 KO plasmid (10 μg) was electroporated into NCI-H1417 or NCI-H146

cells (1 × 10^6) using a NEPA21 (Nepa Gene Co., Ltd., Chiba, Japan) in a 2-mm gap cuvette. The electroporation parameters were as follows: Poring pulse (Voltage: 125 V, Pulse length: 5 ms, Pulse interval: 50 ms, Number of pulses: 2, Decay rate: 10%, Polarity: +) and Transfer pulse (Voltage: 20 V, Pulse length: 50 ms, Pulse interval: 50 ms, Number of pulses: 5, Polarity: ±). Two days later, GFP-positive cells were sorted by BD FACSMelody™ (BD Biosciences, San Jose, CA, USA) and cultured. TAS1440 (300 nM) or DMSO was added the day after sorting. INSM1-KO was confirmed by western blotting (anti-INSM1; Fig. 8b and Supplementary Fig. 13a). LSD1-KO was confirmed by western blotting (anti-LSD1; Fig. 7b and Supplementary Fig. 12b).

Generation of Stable Fluc- and INSM1-expressing SCLC cell lines

For lentivirus preparation, the vector of interest was co-transfected with packaging components VSV-G, gag/pol, and rev into Lenti-X 293T (Clontech) cells at ~70% confluency using Lipofectamine 2000 (Thermo Fisher Scientific). The medium was changed the next day. After 48 h, the viral supernatant was harvested and filtered (0.45 μm). NCI-H146 cells were infected at ~50% confluency and selected with 0.2 μg/mL puromycin for 7 days before analysis. NCI-H196 and NCI-H211 cells were infected similarly and selected with 2 μg/mL and 4 μg/mL blasticidin, respectively, for 10 days before analysis.

***In Vivo* Efficacy Studies**

NCI-H1417, NCI-H146, NCI-H510A, COR-L51 and NCI-H146 INSM1-KO cells were suspended in PBS and mixed 1:1 with Matrigel (Corning, NY, USA). Suspensions were injected subcutaneously into six-week-old male C.B-17 SCID mice (Charles River Laboratories Japan, Inc. and CLEA Japan, Inc.). Upon tumor establishment, mice were randomized into control and experimental groups (n = 4–6 per group) using MiSTAT Grouping to balance mean baseline tumor

volumes. TAS1440 was administered at 16.7 or 50 mg/kg/day. The ORY-1001 dose (0.01–0.03 mg/kg/day) was chosen based on previously reported efficacy in the SCLC PDX models[12]. Tumor volume was calculated as length × width^2 / 2 (length: longest diameter; width: shortest diameter). The maximum tumor diameter permitted was 1.5 cm; all tumors remained ≤1.5 cm. To examine the pulmonary environment, an intrapulmonary implantation model was established: a small skin incision was made on the left chest wall (seventh intercostal space); after exposing the left lung via the pleura, NCI-H146 (1×10^7) cells in 40 µL PBS/Matrigel (3:1) were injected into the lung. Two months later, mice were treated orally with TAS1440 (50 mg/kg/day) or vehicle for 4 weeks. Tumor growth was monitored by micro-CT (SkyScan 1276, Bruker, USA) under anesthesia (50 kV, 200 µA, 2048 × 2048). Mice were euthanized when tumor burden met criteria or at end of treatment; tumors were excised and weighed. Mice were maintained under SPF conditions (20–26 °C; 30–70% humidity; 12-h light cycle) with *ad libitum* CE-2 chow and water. TAS1440 was administered orally once daily for 3 weeks; tumor volume and body weight were measured every 3 days. All animal experiments were approved by the IACUCs of Taiho Pharmaceutical Co., Ltd. (Permit No. AE21-425-01 and 18TB14) and Chiba University (No. A7-284) and conducted in accordance with institutional guidelines.

Docking Simulations

The crystal structure of LSD1 complexed with FAD (PDB 2HKO) was used. Molecular docking between LSD1 and inhibitors was performed using AutoDock Vina (AutoDockTools v1.5.6). Docking scores are reported as binding energies (kcal/mol), with lower values indicating more stable interactions; the lowest-energy pose was selected. Protein–protein docking between LSD1

and INSM1 or SMAD2 was performed using AlphaFold3, and molecular graphics were generated in UCSF ChimeraX.

Survival Analysis

Survival analysis used RNA-seq expression and clinical data from a previously published cohort of patients with SCLC reported by Liu et al.[12]. Overall survival was analyzed using the Kaplan–Meier method and compared by log-rank test. For each gene, patients were stratified into High and Low based on the median TPM. Hazard ratios (HRs) with 95% confidence intervals (CIs) were calculated using the Cox proportional hazards model and expressed as the relative risk of death in the High-expression group versus Low-expression. The log-rank p-value was reported for each gene.

Statistical Analyses

Quantitative data are presented as mean ± SD or mean ± SEM. Comparisons between groups were performed using a two-tailed Student's t-test or one-way analysis of variance unless otherwise specified. Correlations were determined using Pearson's correlation. GraphPad Prism 9 (https://www.graphpad.com) was used for statistical analyses. Statistical significance was set at $P < 0.05$.

Synthesis of TAS1440 Benzoate Salt

Abbreviations: TEA, triethylamine; MeOH, methanol; EtOH, ethanol; HATU, 1-[Bis(dimethylamino)methylene]-1H-1,2,3-triazolo[4,5-b]pyridinium 3-oxide hexafluorophosphate; DMA, *N*,*N*-dimethylacetamide; Ac, acetyl; dppf, 1,1'-

Bis(diphenylphosphino)ferrocene; PPh3, triphenylphosphine; NMR, nuclear magnetic resonance spectroscopy; MS, mass spectrometry; RT, room temperature; aq., aqueous.

General experiments and information: NMR spectra were recorded using a Varian Mercury 400 or Bruker AV Neo 400 NMR spectrometer. Mass spectra were obtained using an ACQUITY QDa Mass Detector (Waters, Framingham, MA, USA).

Reagents and conditions: (a) TEA, HATU, DMA, RT, 1 h, 74%; (b) Pd(PPh3)4, 2 M Na_2CO_3 aq., 1,4-Dioxane, 90 °C, overnight, 90%; (c) Pd(OAc)2, Silica-SMAP, KOAc, 1,4-Dioxane, 150 °C, 18 h, 61%; (d) $PdCl_2$(dppf), 2 M Na_2CO_3 aq., 120 °C, 0.5 h, 78%; (e) 12 M HCl aq., MeOH, RT, 0.5 h, 63%; (f) benzoic acid, ethanol, water, 1 °C, 13 h, 91%.

Step 1: *tert*-Butyl (*S*)-(1-(3-bromo-4-chlorobenzoyl)pyrrolidin-3-yl)carbamate (**S2**)

3-Bromo-4-chloro-benzoic acid (**S1**) (10 g) was dissolved in DMA (85 mL). HATU (24 g), TEA (12 mL), and *tert*-Butyl *N*-[(3*S*)-pyrrolidin-3-yl]carbamate (**S1.1**) (8.7 g) were added to the solution, which was stirred at room temperature for 1 h. Ethyl acetate was added to the mixture, and the resulting mixture was washed with water and brine. The organic layer was dried over anhydrous sodium sulfate, and the solvent was evaporated. The residue was purified by chromatography using a silica-gel column (mobile phase: hexane/ethyl acetate) to obtain the title compound (12.7 g) as a solid. ESI MS *m/z* 403, 405, 407 $[M+H]^+$.

Step 2: *tert*-Butyl *N*-[(3*S*)-1-[4-chloro-3-(4-cyano-3-fluoro-phenyl)benzoyl]pyrrolidin-3-yl]carbamate (**S3**).

tert-Butyl (*S*)-(1-(3-bromo-4-chlorobenzoyl)pyrrolidin-3-yl)carbamate (**S2**) (14 g) was dissolved in 1,4-dioxane (87 mL). (4-Cyano-3-fluoro-phenyl)boronic acid (**S2.2**) (6.3 g), $Pd(PPh_3)_4$ (1.2 g),

and 2 M Na_2CO_3 aqueous solution (43 mL) were added to the solution and stirred at 90 °C overnight. Ethyl acetate was added to the mixture, and the resulting mixture was washed with water and brine. The organic layer was dried over anhydrous sodium sulfate, and the solvent was evaporated. The residue was purified by chromatography using a silica-gel column (mobile phase: hexane/ethyl acetate) to obtain the title compound (13.9 g) as a solid. ESI MS *m/z* 444, 446 $[M+H]^+$.

Step 3: *tert*-Butyl *N*-[(3*S*)-1-[3-(4-cyano-3-fluoro-phenyl)-4-(4,4,5,5-tetramethyl-1,3,2-dioxaborolan-2-yl)benzoyl]pyrrolidin-3-yl]carbamate (**S4**).

tert-Butyl *N*-[(3*S*)-1-[4-chloro-3-(4-cyano-3-fluoro-phenyl)benzoyl]pyrrolidin-3-yl]carbamate (**S3**) (4 g) was dissolved in 1,4-dioxane (45 mL). At room temperature, $Pd(OAc)_2$ (0.40 g), KOAc (2.7 g), bis(pinacolato)diboron (4.6 g), and Silica-SMAP (0.72 g) were added to the mixture and stirred at 150 °C for 18 h. The mixture was cooled to room temperature. Subsequently, the mixture was filtered, and filtrate evaporated. The resulting residue was purified by chromatography using a silica-gel column (mobile phase: hexane/ethyl acetate) to obtain the title compound (2.95 g) as a solid. ESI MS *m/z* 536 $[M+H]^+$.

Step 4: *tert*-Butyl *N*-[(3*S*)-1-[3-(4-cyano-3-fluoro-phenyl)-4-[2-fluoro-4-(2-hydroxy-2-methyl-propyl)phenyl]benzoyl]pyrrolidin-3-yl] carbamate (**S5**).

tert-Butyl *N*-[(3*S*)-1-[3-(4-cyano-3-fluoro-phenyl)-4-(4,4,5,5-tetramethyl-1,3,2-dioxaborolan-2-yl)benzoyl]pyrrolidin-3-yl]carbamate (**S4**) (8.00 g) and 1-(4-bromo-3-fluoro-phenyl)-2-methyl-propan-2-ol (**S4.1**) (4.43 g) were dissolved in 1,4-dioxane (75 mL). $PdCl_2$(dppf) (273 mg) and 2 M Na_2CO_3 aq. (37 mL) were added to the mixture, which was stirred at 120 °C for 0.5 h. The mixture was cooled to RT. The reaction mixture was filtered, and filtrate evaporated. Ethyl

acetate was added to the resulting mixture. The organic layer was washed with water and brine, dried over anhydrous sodium sulfate, and the filtrate was evaporated. The residue was purified by chromatography using a silica-gel column (mobile phase: chloroform/methanol) to obtain the title compound (6.70 g) as a solid. ESI MS *m/z* 576 $[M+H]^+$.

Step 5: 4-[5-[(3*S*)-3-Aminopyrrolidine-1-carbonyl]-2-[2-fluoro-4-(2-hydroxy-2-methyl-propyl)phenyl]phenyl]-2-fluoro-benzonitrile (**TAS1440**).

tert-Butyl *N*-[(3*S*)-1-[3-(4-cyano-3-fluoro-phenyl)-4-[2-fluoro-4-(2-hydroxy-2-methyl-propyl)phenyl]benzoyl]pyrrolidin-3-yl] carbamate (**S5**) (6.70 g) was dissolved in methanol (67 mL). A 12 M aqueous HCl solution (67 mL) was added to the solution and stirred at RT for 30 min. The reaction mixture was neutralized by adding water (67 mL) and 2 M aqueous sodium hydroxide (500 mL) (the solution was confirmed to be basic using a pH indicator). Chloroform was added to the mixture, and the organic layer was washed with water and brine and dried over anhydrous sodium sulfate. The filtrate was evaporated to obtain the title compound (4.50 g) as a solid.

^{1}H-NMR (500 MHz, DMSO-d_6) δ: 7.79 (1H, t, *J* = 7.5 Hz), 7.70–7.67 (1H, m), 7.63 (1H, dd, *J* = 6.6, 1.5 Hz), 7.52 (1H, d, *J* = 8.1 Hz), 7.27 (1H, d, *J* = 10.3 Hz), 7.21 (1H, t, *J* = 7.9 Hz), 7.14 (1H, dd, *J* = 8.1, 1.5 Hz), 7.06 (1H, d, *J* = 7.7 Hz), 6.95 (1H, d, *J* = 11.4 Hz), 4.39 (1H, s), 3.68–3.55 (2H, m), 3.54–3.41 (2H, m), 3.21–3.12 (1H, m), 2.65 (2H, s), 2.03–1.88 (1H, m), 1.75 (2H, s), 1.70–1.59 (1H, m), 1.04 (6H, s); ESI MS *m/z* 476 $[M+H]^+$.

Step 6: 4-[5-[(3*S*)-3-Aminopyrrolidine-1-carbonyl]-2-[2-fluoro-4-(2-hydroxy-2-methyl-propyl)phenyl]phenyl]-2-fluoro-benzonitrile benzoate salt (**TAS1440 benzoate salt**).

Ethanol (42 mL) and water (18 mL) were added to 4-[5-[(3*S*)-3-aminopyrrolidine-1-carbonyl]-2-[2-fluoro-4-(2-hydroxy-2-methyl-propyl)phenyl]phenyl]-2-fluoro-benzonitrile (**TAS1440**) (10 g) and benzoic acid (2.57 g), and stirred at 60 °C for 20 min to dissolve the mixture. Subsequently, water (45 mL) was added dropwise to the solution for 3 min at 60 °C and cooled to 1 °C. The suspension was then stirred at 1 °C for 13 h. The resulting precipitate was collected by filtration, washed with a mixture of ethanol (6 mL) and water (14 mL), and dried to obtain the title compound (11.5 g) as an off-white solid.

^{1}H NMR (400 MHz, DMSO-*d6*) δ 7.90 (d, *J* = 7.29 Hz, 2H), 7.78 (t, *J* = 7.15 Hz, 1H), 7.61–7.72 (m, 2H), 7.45–7.55 (m, 2H), 7.36–7.42 (m, 2H), 7.17–7.29 (m, 2H), 7.13 (d, *J* = 8.43 Hz, 1H), 7.06 (dd, *J* = 1.28, 7.88 Hz, 1H), 6.95 (dd, *J* = 1.10, 11.36 Hz, 1H), 3.26–3.80 (m, 5H), 2.65 (s, 2H), 1.99–2.14 (m, 1H), 1.75–1.92 (m, 1H), 1.04 (s, 6H); ESI MS *m/z* 476 $[M+H]^{+}$.

Data Availability

Any additional information required to reanalyze the data reported in this paper is available from the lead contact upon request. The RNA-seq data generated in this study have been deposited in the Gene Expression Omnibus (GEO) database under accession code GSE272002 and the ChIP-seq data generated in this study have been deposited in the GEO database under accession code GSE272003. The mass spectrometry proteomics data were deposited in the Japan Proteome Standard repository/database JPST003190. Proteomics data supporting the findings of this study are available within the article and in Supplementary Data 1. Source data are provided with this paper.

Code Availability

No custom code was generated in this study.

References

1 Rudin, C. M. *et al.* Molecular subtypes of small cell lung cancer: a synthesis of human and mouse model data. *Nat Rev Cancer* **19**, 289-297 (2019). https://doi.org/10.1038/s41568-019-0133-9

2 Franco, F. *et al.* Epidemiology, treatment, and survival in small cell lung cancer in Spain: Data from the Thoracic Tumor Registry. *PLoS One* **16**, e0251761 (2021). https://doi.org/10.1371/journal.pone.0251761

3 Rekhtman, N. All That Is Small Is Not a Small-Cell Carcinoma: Thoracic SMARCA4-Deficient Undifferentiated Tumors Masquerading as SCLC. *Clinical cancer research* **30**, 1708-1711 (2024). https://doi.org/10.1158/1078-0432.CCR-24-0227

4 Gay, C. M. *et al.* Patterns of transcription factor programs and immune pathway activation define four major subtypes of SCLC with distinct therapeutic vulnerabilities. *Cancer Cell* **39**, 346-360 e347 (2021). https://doi.org/10.1016/j.ccell.2020.12.014

5 Lim, J. S. *et al.* Intratumoural heterogeneity generated by Notch signalling promotes small-cell lung cancer. *Nature* **545**, 360-364 (2017). https://doi.org/10.1038/nature22323

6 Katoh, M. & Katoh, M. Precision medicine for human cancers with Notch signaling dysregulation (Review). *Int J Mol Med* **45**, 279-297 (2020). https://doi.org/10.3892/ijmm.2019.4418

7 Mulligan, P. *et al.* A SIRT1-LSD1 corepressor complex regulates Notch target gene expression and development. *Mol Cell* **42**, 689-699 (2011). https://doi.org/10.1016/j.molcel.2011.04.020

8 Perillo, B., Tramontano, A., Pezone, A. & Migliaccio, A. LSD1: more than demethylation of histone lysine residues. *Exp Mol Med* **52**, 1936-1947 (2020). https://doi.org/10.1038/s12276-020-00542-2

9 Kim, S. A., Zhu, J., Yennawar, N., Eek, P. & Tan, S. Crystal Structure of the LSD1/CoREST Histone Demethylase Bound to Its Nucleosome Substrate. *Mol Cell* **78**, 903-914 e904 (2020). https://doi.org/10.1016/j.molcel.2020.04.019

10 Wang, Y. *et al.* LSD1 is a subunit of the NuRD complex and targets the metastasis programs in breast cancer. *Cell* **138**, 660-672 (2009). https://doi.org/10.1016/j.cell.2009.05.050

11 Fang, Y., Liao, G. & Yu, B. LSD1/KDM1A inhibitors in clinical trials: advances and prospects. *J Hematol Oncol* **12**, 129 (2019). https://doi.org/10.1186/s13045-019-0811-9

12 Augert, A. *et al.* Targeting NOTCH activation in small cell lung cancer through LSD1 inhibition. *Sci Signal* **12** (2019). https://doi.org/10.1126/scisignal.aau2922

13 Noce, B., Di Bello, E., Fioravanti, R. & Mai, A. LSD1 inhibitors for cancer treatment: Focus on multi-target agents and compounds in clinical trials. *Front Pharmacol* **14**, 1120911 (2023). https://doi.org/10.3389/fphar.2023.1120911

14 Bhansali, R. S., Pratz, K. W. & Lai, C. Recent advances in targeted therapies in acute myeloid leukemia. *J Hematol Oncol* **16**, 29 (2023). https://doi.org/10.1186/s13045-023-01424-6

15 Kumalo, H. M., Bhakat, S. & Soliman, M. E. Theory and applications of covalent docking in drug discovery: merits and pitfalls. *Molecules* **20**, 1984-2000 (2015). https://doi.org/10.3390/molecules20021984

16 Kanouni, T. *et al.* Discovery of CC-90011: A Potent and Selective Reversible Inhibitor of Lysine Specific Demethylase 1 (LSD1). *J Med Chem* **63**, 14522-14529 (2020). https://doi.org/10.1021/acs.jmedchem.0c00978

17 Shen, L. *et al.* Combination Therapy and Dual-Target Inhibitors Based on LSD1: New Emerging Tools in Cancer Therapy. *J Med Chem* **67**, 922-951 (2024). https://doi.org/10.1021/acs.jmedchem.3c02133

18 Fiskus, W. *et al.* Highly effective combination of LSD1 (KDM1A) antagonist and pan-histone deacetylase inhibitor against human AML cells. *Leukemia* **28**, 2155-2164 (2014). https://doi.org/10.1038/leu.2014.119

19 Batlle, E. & Massague, J. Transforming Growth Factor-beta Signaling in Immunity and Cancer. *Immunity* **50**, 924-940 (2019). https://doi.org/10.1016/j.immuni.2019.03.024

20 Bray, S. J. Notch signalling in context. *Nat Rev Mol Cell Biol* **17**, 722-735 (2016). https://doi.org/10.1038/nrm.2016.94

21 Nguyen, E. M. *et al.* Targeting Lysine-Specific Demethylase 1 Rescues Major Histocompatibility Complex Class I Antigen Presentation and Overcomes Programmed Death-Ligand 1 Blockade Resistance in SCLC. *J Thorac Oncol* **17**, 1014-1031 (2022). https://doi.org/10.1016/j.jtho.2022.05.014

22 Alagarswamy, K. *et al.* Region-specific alteration of histone modification by LSD1 inhibitor conjugated with pyrrole-imidazole polyamide. *Oncotarget* **9**, 29316-29335 (2018). https://doi.org/10.18632/oncotarget.25451

23 Sonnemann, J. *et al.* LSD1 (KDM1A)-independent effects of the LSD1 inhibitor SP2509 in cancer cells. *Br J Haematol* **183**, 494-497 (2018). https://doi.org/10.1111/bjh.14983

24 Liu, Q. *et al.* Proteogenomic characterization of small cell lung cancer identifies biological insights and subtype-specific therapeutic strategies. *Cell* **187**, 184-203 e128 (2024). https://doi.org/10.1016/j.cell.2023.12.004

25 Zheng, Y. C. *et al.* Irreversible LSD1 Inhibitors: Application of Tranylcypromine and Its Derivatives in Cancer Treatment. *Curr Top Med Chem* **16**, 2179-2188 (2016). https://doi.org/10.2174/1568026616666160216154042

26 Maes, T. *et al.* ORY-1001, a Potent and Selective Covalent KDM1A Inhibitor, for the Treatment of Acute Leukemia. *Cancer Cell* **33**, 495-511 e412 (2018). https://doi.org/10.1016/j.ccell.2018.02.002

27 Bauer, T. M. *et al.* Phase I, Open-Label, Dose-Escalation Study of the Safety, Pharmacokinetics, Pharmacodynamics, and Efficacy of GSK2879552 in Relapsed/Refractory SCLC. *J Thorac Oncol* **14**, 1828-1838 (2019). https://doi.org/10.1016/j.jtho.2019.06.021

28 Roboz, G. J. *et al.* Phase I trials of the lysine-specific demethylase 1 inhibitor, GSK2879552, as mono- and combination-therapy in relapsed/refractory acute myeloid leukemia or high-risk myelodysplastic syndromes. *Leuk Lymphoma* **63**, 463-467 (2022). https://doi.org/10.1080/10428194.2021.2012667

29 Salamero, O. *et al.* First-in-Human Phase I Study of Iadademstat (ORY-1001): A First-in-Class Lysine-Specific Histone Demethylase 1A Inhibitor, in Relapsed or Refractory Acute Myeloid Leukemia. *J Clin Oncol* **38**, 4260-4273 (2020). https://doi.org/10.1200/JCO.19.03250

30 Hollebecque, A. *et al.* Phase I Study of Lysine-Specific Demethylase 1 Inhibitor, CC-90011, in Patients with Advanced Solid Tumors and Relapsed/Refractory Non-Hodgkin Lymphoma. *Clin Cancer Res* **27**, 438-446 (2021). https://doi.org/10.1158/1078-0432.CCR-20-2380

31 Hollebecque, A. *et al.* Clinical activity of CC-90011, an oral, potent, and reversible LSD1 inhibitor, in advanced malignancies. *Cancer* **128**, 3185-3195 (2022). https://doi.org/10.1002/cncr.34366

32 Takagi, S. *et al.* LSD1 Inhibitor T-3775440 Inhibits SCLC Cell Proliferation by Disrupting LSD1 Interactions with SNAG Domain Proteins INSM1 and GFI1B. *Cancer Res* **77**, 4652-4662 (2017). https://doi.org/10.1158/0008-5472.CAN-16-3502

33 Osipovich, A. B. *et al.* Insm1 promotes endocrine cell differentiation by modulating the expression of a network of genes that includes Neurog3 and Ripply3. *Development* **141**, 2939-2949 (2014). https://doi.org/10.1242/dev.104810

34 Mahalakshmi, B., Baskaran, R., Shanmugavadivu, M., Nguyen, N. T. & Velmurugan, B. K. Insulinoma-associated protein 1 (INSM1): a potential biomarker and therapeutic target for neuroendocrine tumors. *Cell Oncol (Dordr)* **43**, 367-376 (2020). https://doi.org/10.1007/s13402-020-00505-9

35 Jia, S., Wildner, H. & Birchmeier, C. Insm1 controls the differentiation of pulmonary neuroendocrine cells by repressing Hes1. *Dev Biol* **408**, 90-98 (2015). https://doi.org/10.1016/j.ydbio.2015.10.009

36 Breslin, M. B., Zhu, M., Notkins, A. L. & Lan, M. S. Neuroendocrine differentiation factor, IA-1, is a transcriptional repressor and contains a specific DNA-binding domain: identification of consensus IA-1 binding sequence. *Nucleic Acids Res* **30**, 1038-1045 (2002). https://doi.org/10.1093/nar/30.4.1038

37 Noguchi, M., Furukawa, K. T. & Morimoto, M. Pulmonary neuroendocrine cells: physiology, tissue homeostasis and disease. *Dis Model Mech* **13** (2020). https://doi.org/10.1242/dmm.046920

38 Meuwissen, R. *et al.* Induction of small cell lung cancer by somatic inactivation of both Trp53 and Rb1 in a conditional mouse model. *Cancer Cell* **4**, 181-189 (2003). https://doi.org/10.1016/s1535-6108(03)00220-4

39 Sutherland, K. D. *et al.* Cell of origin of small cell lung cancer: inactivation of Trp53 and Rb1 in distinct cell types of adult mouse lung. *Cancer Cell* **19**, 754-764 (2011). https://doi.org/10.1016/j.ccr.2011.04.019

40 Wooten, D. J. *et al.* Systems-level network modeling of Small Cell Lung Cancer subtypes identifies master regulators and destabilizers. *PLoS Comput Biol* **15**, e1007343 (2019). https://doi.org/10.1371/journal.pcbi.1007343

41 Ireland, A. S. *et al.* MYC Drives Temporal Evolution of Small Cell Lung Cancer Subtypes by Reprogramming Neuroendocrine Fate. *Cancer Cell* **38**, 60-78 e12 (2020). https://doi.org/10.1016/j.ccell.2020.05.001

42 Bozec, D. *et al.* Akaluc bioluminescence offers superior sensitivity to track in vivo glioma expansion. *Neurooncol Adv* **2**, vdaa134 (2020). https://doi.org/10.1093/noajnl/vdaa134

Editor Summary:
Existing inhibitors for lysine-specific histone demethylase 1A (LSD1), a key driver for small cell lung cancer (SCLC) carcinogenesis, have notable limitations. Here, the authors employ structure-based engineering to develop a histone H3-competitive LSD1 inhibitor to enhance specificity and reduce off-target effects in SCLC cells through transcriptional regulation and epigenetic reprogramming.
Peer Review Information:
Nature Communications thanks Hongbin Ji, Carl Gay, Gangadhara Sareddy, Andrea Mattevi and the other anonymous reviewer for their contribution to the peer review of this work. [A peer review file is available.]

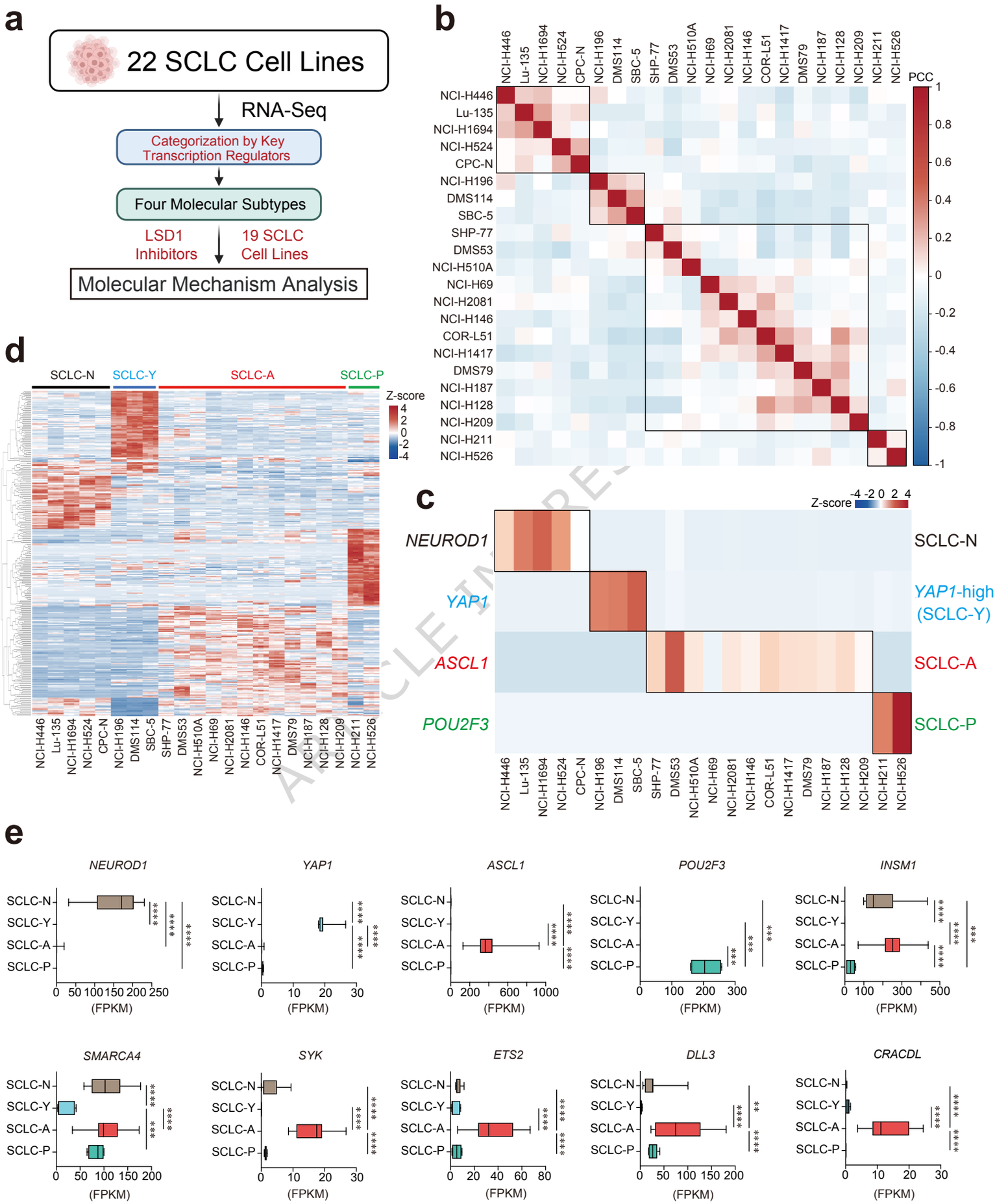
a
22 SCLC Cell Lines
RNA-Seq
Categorization by Key Transcription Regulators
Four Molecular Subtypes
LSD1 Inhibitors
19 SCLC Cell Lines
Molecular Mechanism Analysis
b
PCC
c
Z-score
NEUROD1
YAP1
ASCL1
POU2F3
SCLC-N
YAP1-high (SCLC-Y)
SCLC-A
SCLC-P
d
SCLC-N
SCLC-Y
SCLC-A
SCLC-P
Z-score
e
NEUROD1
YAP1
ASCL1
POU2F3
INSM1
SMARCA4
SYK
ETS2
DLL3
CRACDL
(FPKM)

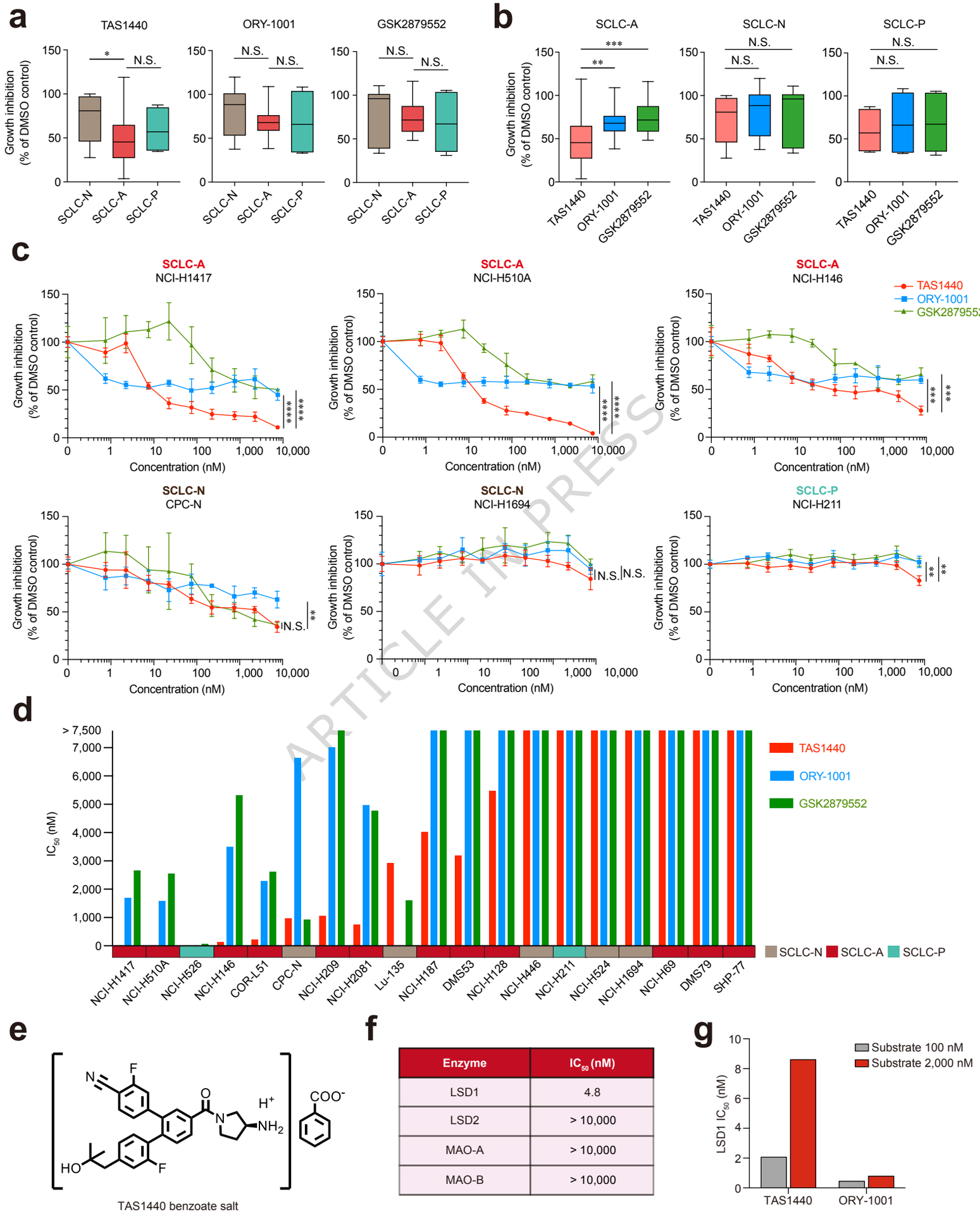

Enzyme	IC_{50} (nM)
LSD1	4.8
LSD2	> 10,000
MAO-A	> 10,000
MAO-B	> 10,000

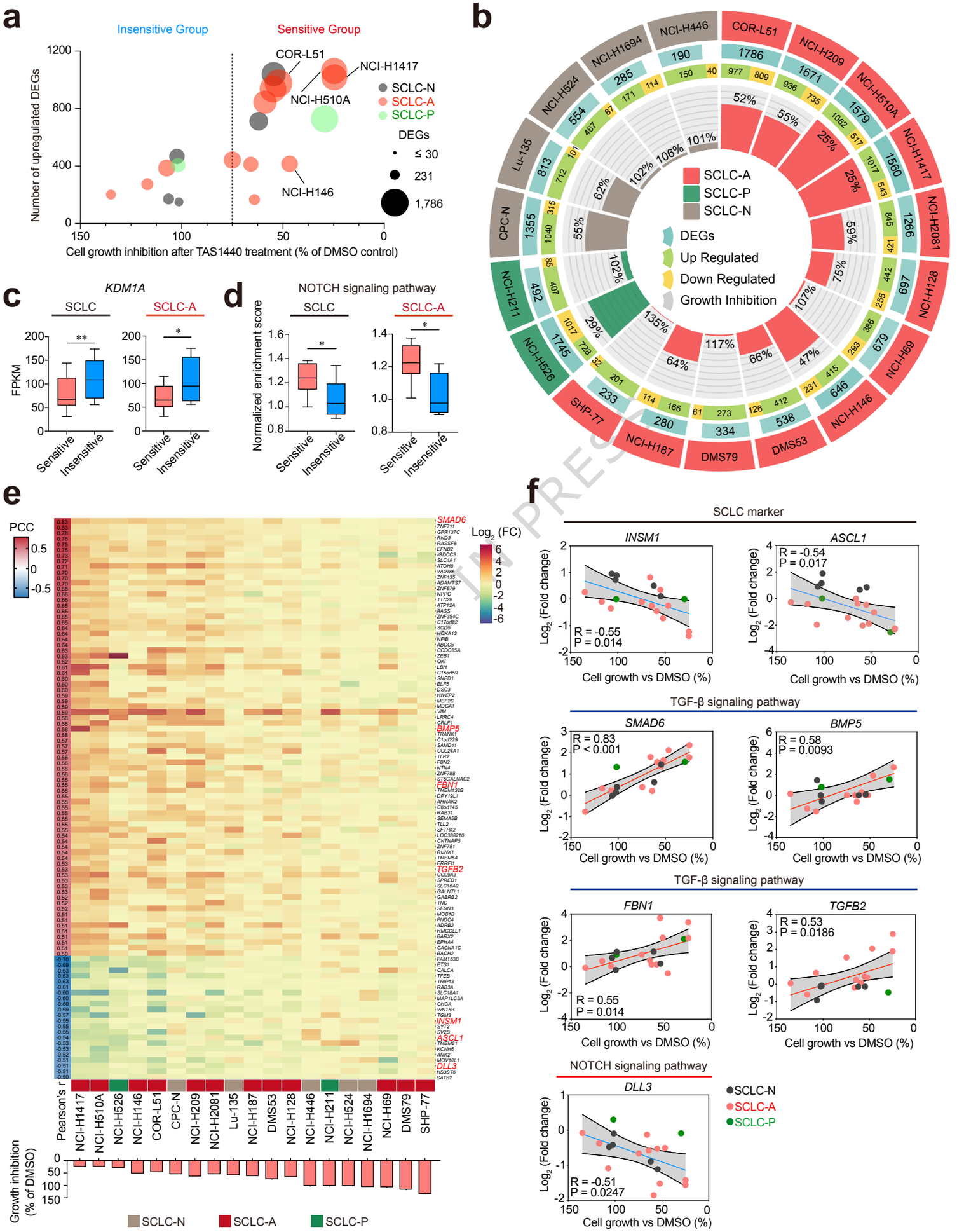
a
Insensitive Group
Sensitive Group
Number of upregulated DEGs
Cell growth inhibition after TAS1440 treatment (% of DMSO control)
COR-L51
NCI-H1417
NCI-H510A
NCI-H146
SCLC-N
SCLC-A
SCLC-P
DEGs
≤ 30
231
1,786
b
SCLC-A
SCLC-P
SCLC-N
DEGs
Up Regulated
Down Regulated
Growth Inhibition
c
KDM1A
SCLC
SCLC-A
FPKM
Sensitive
Insensitive
d
NOTCH signaling pathway
Normalized enrichment score
e
PCC
Log2 (FC)
Pearson's r
Growth inhibition (% of DMSO)
SCLC-N
SCLC-A
SCLC-P
f
SCLC marker
INSM1
ASCL1
TGF-β signaling pathway
SMAD6
BMP5
FBN1
TGFB2
NOTCH signaling pathway
DLL3
Log2 (Fold change)
Cell growth vs DMSO (%)

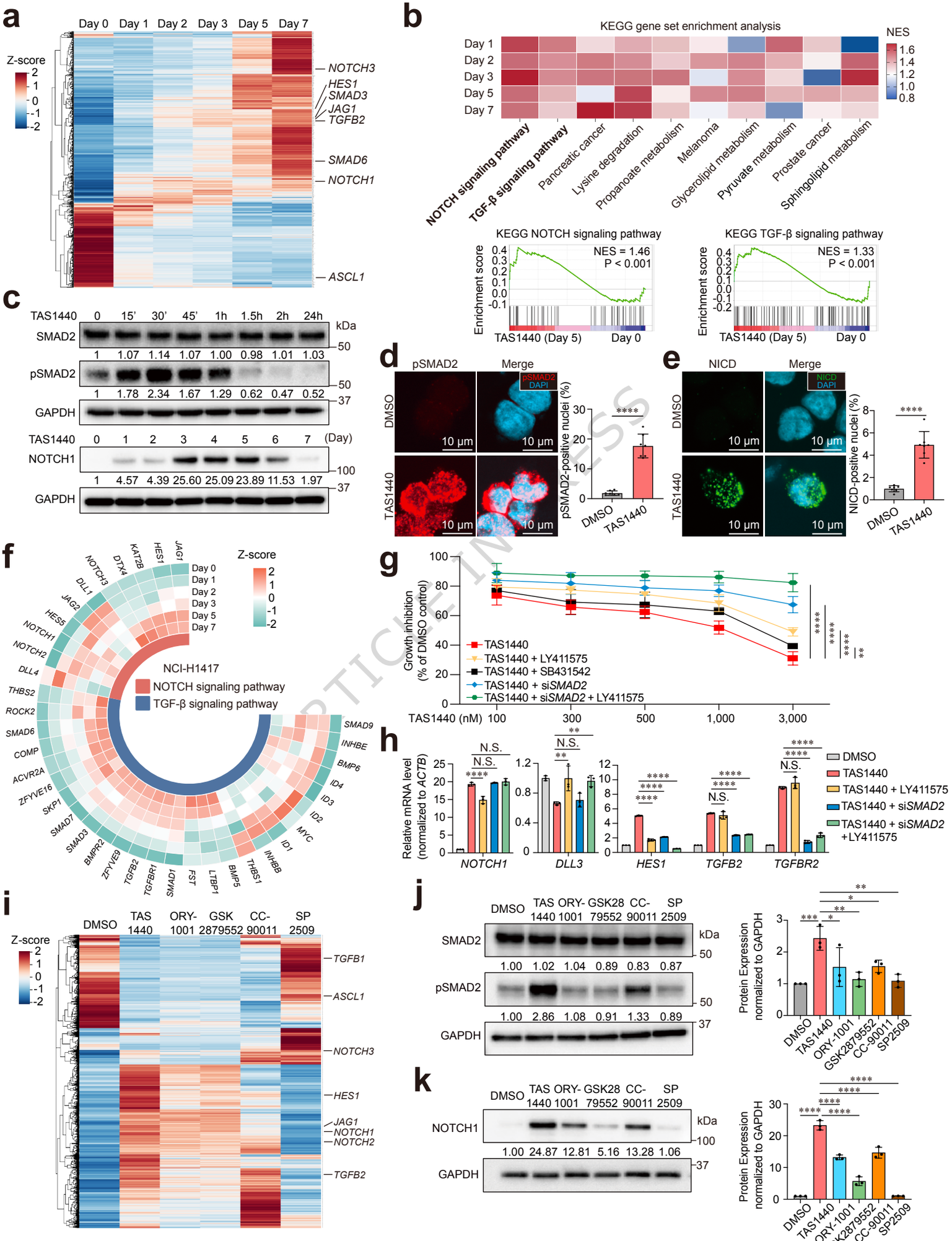
a
Day 0 Day 1 Day 2 Day 3 Day 5 Day 7
Z-score
2
1
0
-1
-2
NOTCH3
HES1
SMAD3
JAG1
TGFB2
SMAD6
NOTCH1
ASCL1
b
KEGG gene set enrichment analysis
NES
1.6
1.4
1.2
1.0
0.8
Day 1
Day 2
Day 3
Day 5
Day 7
NOTCH signaling pathway
TGF-β signaling pathway
Pancreatic cancer
Lysine degradation
Propanoate metabolism
Melanoma
Glycerolipid metabolism
Pyruvate metabolism
Prostate cancer
Sphingolipid metabolism
KEGG NOTCH signaling pathway
NES = 1.46
P < 0.001
Enrichment score
TAS1440 (Day 5)
Day 0
KEGG TGF-β signaling pathway
NES = 1.33
P < 0.001
Enrichment score
TAS1440 (Day 5)
Day 0
c
TAS1440 0 15' 30' 45' 1h 1.5h 2h 24h
kDa
SMAD2
50
1 1.07 1.14 1.07 1.00 0.98 1.01 1.03
pSMAD2
50
1 1.78 2.34 1.67 1.29 0.62 0.47 0.52
GAPDH
37
TAS1440 0 1 2 3 4 5 6 7 (Day)
NOTCH1
100
1 4.57 4.39 25.60 25.09 23.89 11.53 1.97
GAPDH
37
d
pSMAD2
Merge
pSMAD2
DAPI
DMSO
TAS1440
10 μm
pSMAD2-positive nuclei (%)
****
DMSO
TAS1440
e
NICD
Merge
NICD
DAPI
DMSO
TAS1440
10 μm
NICD-positive nuclei (%)
****
DMSO
TAS1440
f
Z-score
2
1
0
-1
-2
Day 0
Day 1
Day 2
Day 3
Day 5
Day 7
NCI-H1417
NOTCH signaling pathway
TGF-β signaling pathway
JAG1
HES1
KAT2B
DTX4
NOTCH3
DLL1
JAG2
HES5
NOTCH1
NOTCH2
DLL4
THBS2
ROCK2
SMAD6
COMP
ACVR2A
ZFYVE16
SKP1
SMAD7
SMAD3
BMPR2
ZFYVE9
TGFB2
TGFBR1
SMAD1
FST
LTBP1
BMP5
THBS1
INHBB
ID1
MYC
ID2
ID3
ID4
BMP6
INHBE
SMAD9
g
Growth inhibition (% of DMSO control)
TAS1440
TAS1440 + LY411575
TAS1440 + SB431542
TAS1440 + siSMAD2
TAS1440 + siSMAD2 + LY411575
TAS1440 (nM) 100 300 500 1,000 3,000
h
Relative mRNA level (normalized to ACTB)
N.S.
****
**
NOTCH1
DLL3
HES1
TGFB2
TGFBR2
DMSO
TAS1440
TAS1440 + LY411575
TAS1440 + siSMAD2
TAS1440 + siSMAD2 +LY411575
i
DMSO
TAS 1440
ORY-1001
GSK 2879552
CC-90011
SP 2509
Z-score
2
1
0
-1
-2
TGFB1
ASCL1
NOTCH3
HES1
JAG1
NOTCH1
NOTCH2
TGFB2
j
DMSO
TAS 1440
ORY-1001
GSK 2879552
CC-90011
SP 2509
SMAD2
kDa
50
1.00 1.02 1.04 0.89 0.83 0.87
pSMAD2
50
1.00 2.86 1.08 0.91 1.33 0.89
GAPDH
37
Protein Expression normalized to GAPDH
DMSO
TAS1440
ORY-1001
GSK2879552
CC-90011
SP2509
k
DMSO
TAS 1440
ORY-1001
GSK 79552
CC-90011
SP 2509
NOTCH1
kDa
100
1.00 24.87 12.81 5.16 13.28 1.06
GAPDH
37
Protein Expression normalized to GAPDH
DMSO
TAS1440
ORY-1001
GSK2879552
CC-90011
SP2509

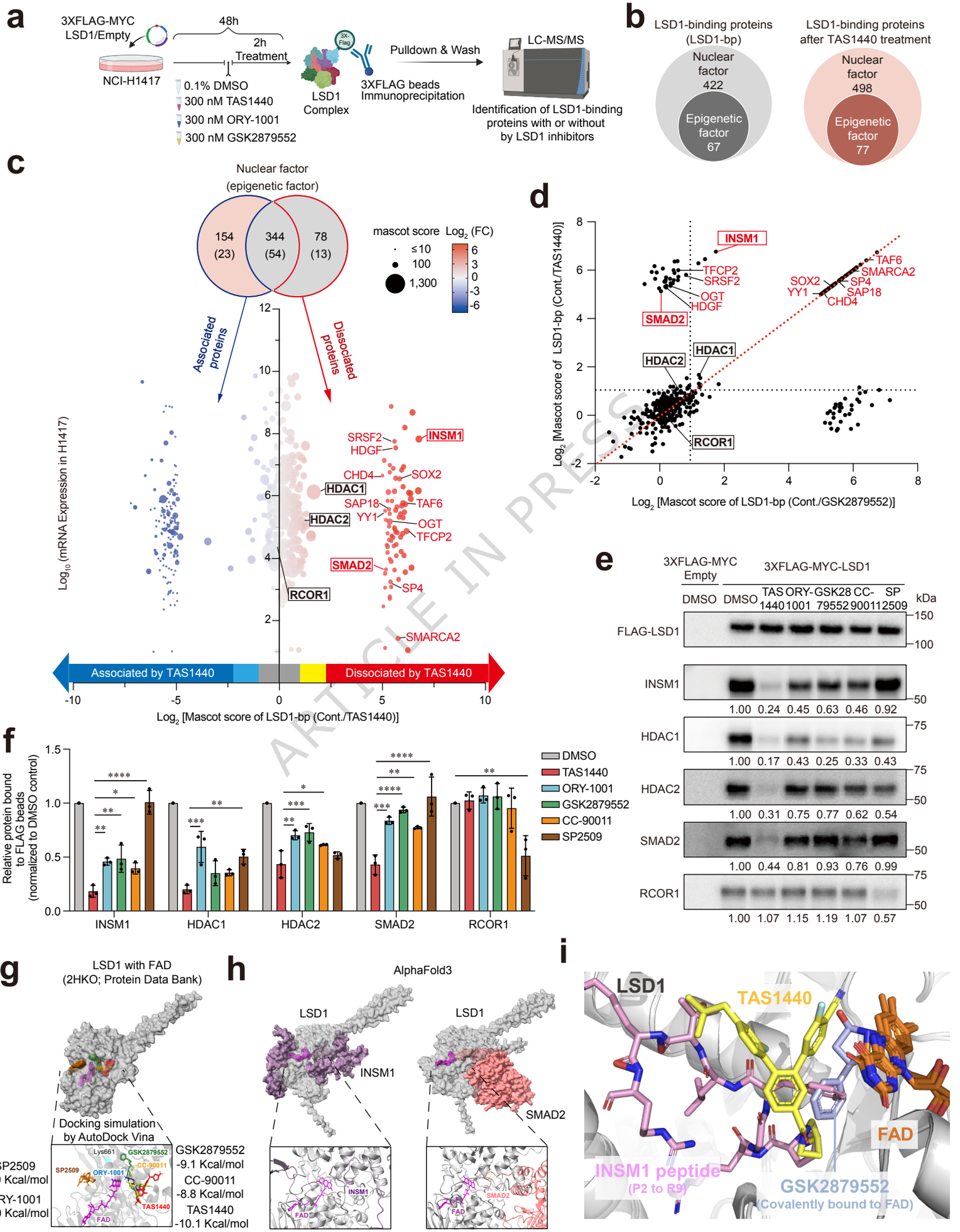

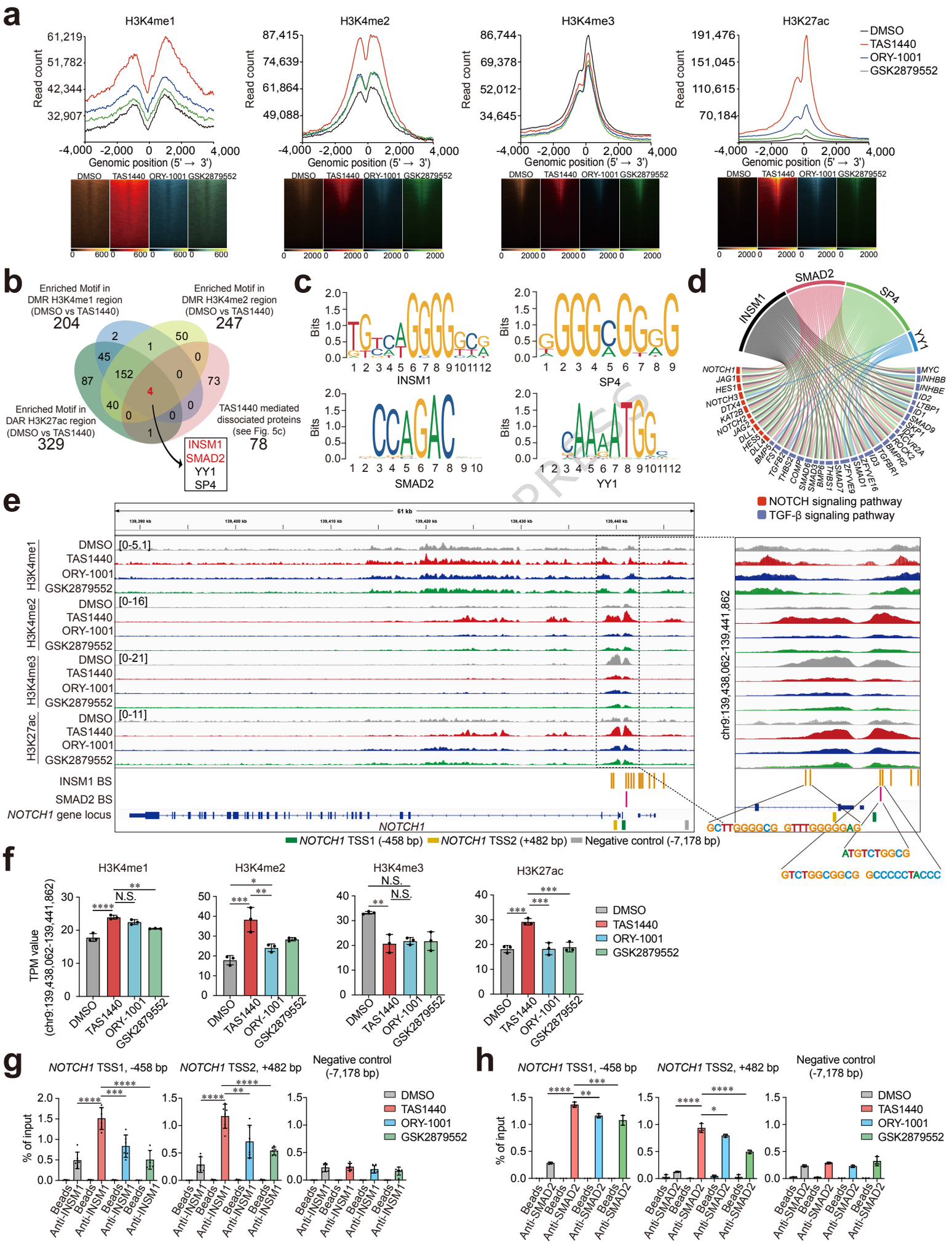
a
H3K4me1
H3K4me2
H3K4me3
H3K27ac
Read count
Genomic position (5' → 3')
DMSO
TAS1440
ORY-1001
GSK2879552
b
Enriched Motif in DMR H3K4me1 region (DMSO vs TAS1440)
204
Enriched Motif in DMR H3K4me2 region (DMSO vs TAS1440)
247
Enriched Motif in DAR H3K27ac region (DMSO vs TAS1440)
329
TAS1440 mediated dissociated proteins (see Fig. 5c)
78
INSM1
SMAD2
YY1
SP4
c
INSM1
SP4
SMAD2
YY1
Bits
d
SMAD2
SP4
INSM1
YY1
NOTCH signaling pathway
TGF-β signaling pathway
e
61 kb
DMSO
TAS1440
ORY-1001
GSK2879552
H3K4me1
H3K4me2
H3K3me3
H3K27ac
INSM1 BS
SMAD2 BS
NOTCH1 gene locus
NOTCH1
NOTCH1 TSS1 (-458 bp)
NOTCH1 TSS2 (+482 bp)
Negative control (-7,178 bp)
GCTTGGGGCG GTTTGGGGGAG
ATGTCTGGCG
GTCTGGCGGCG GCCCCCTACCC
f
H3K4me1
H3K4me2
H3K4me3
H3K27ac
TPM value (chr9:139,438,062-139,441,862)
N.S.
g
NOTCH1 TSS1, -458 bp
NOTCH1 TSS2, +482 bp
Negative control (-7,178 bp)
% of input
Beads
Anti-INSM1
h
Anti-SMAD2

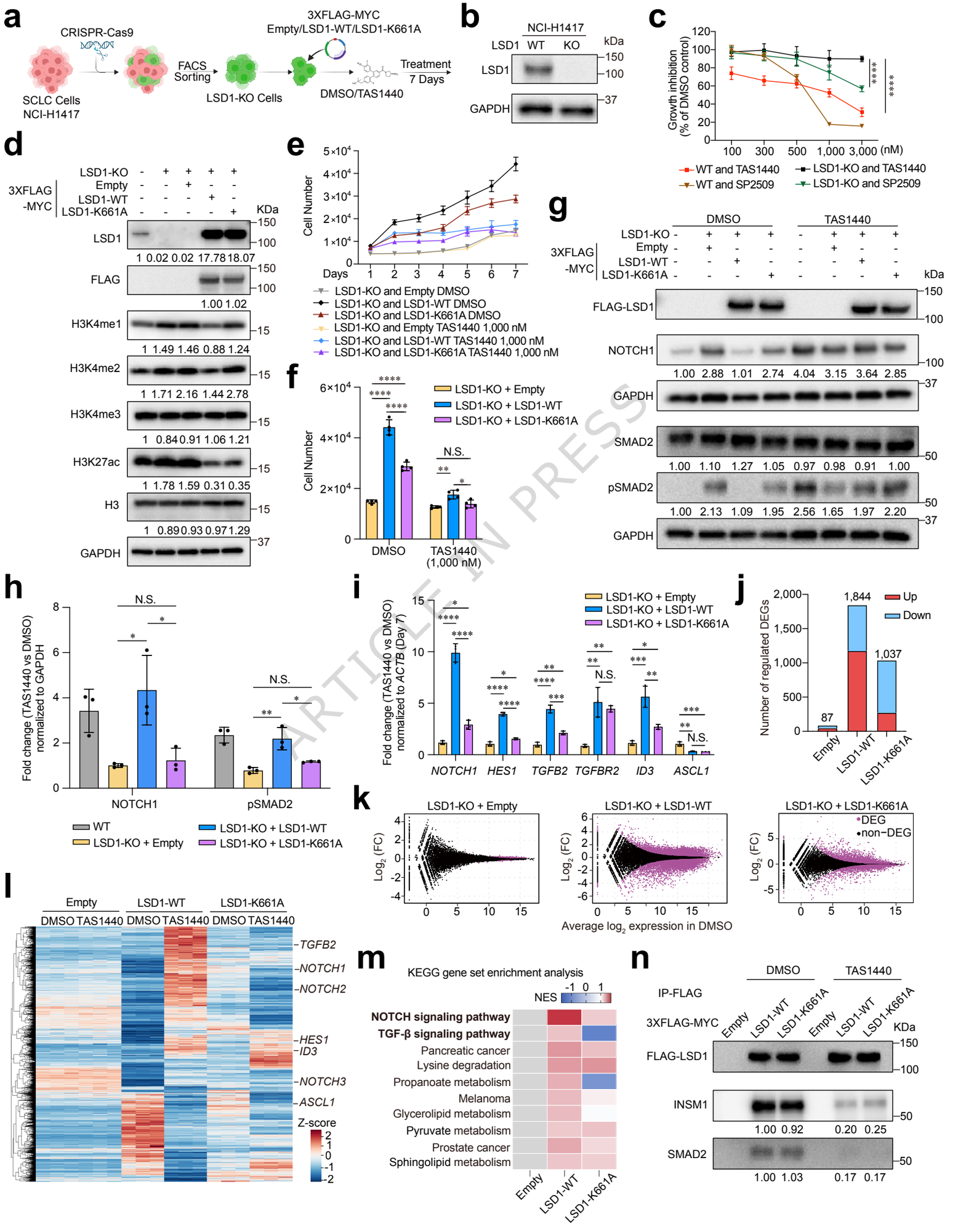
a
CRISPR-Cas9
SCLC Cells
NCI-H1417
FACS Sorting
LSD1-KO Cells
3XFLAG-MYC
Empty/LSD1-WT/LSD1-K661A
DMSO/TAS1440
Treatment 7 Days
b
NCI-H1417
LSD1 WT KO
kDa
LSD1
GAPDH
c
Growth inhibition (% of DMSO control)
(nM)
WT and TAS1440
LSD1-KO and TAS1440
WT and SP2509
LSD1-KO and SP2509
d
3XFLAG -MYC
LSD1-KO
Empty
LSD1-WT
LSD1-K661A
LSD1
FLAG
H3K4me1
H3K4me2
H3K4me3
H3K27ac
H3
GAPDH
e
Cell Number
Days
LSD1-KO and Empty DMSO
LSD1-KO and LSD1-WT DMSO
LSD1-KO and LSD1-K661A DMSO
LSD1-KO and Empty TAS1440 1,000 nM
LSD1-KO and LSD1-WT TAS1440 1,000 nM
LSD1-KO and LSD1-K661A TAS1440 1,000 nM
f
Cell Number
LSD1-KO + Empty
LSD1-KO + LSD1-WT
LSD1-KO + LSD1-K661A
N.S.
DMSO
TAS1440 (1,000 nM)
g
DMSO
TAS1440
3XFLAG -MYC
FLAG-LSD1
NOTCH1
GAPDH
SMAD2
pSMAD2
h
Fold change (TAS1440 vs DMSO) normalized to GAPDH
N.S.
NOTCH1
pSMAD2
WT
LSD1-KO + Empty
LSD1-KO + LSD1-WT
LSD1-KO + LSD1-K661A
i
Fold change (TAS1440 vs DMSO) normalized to ACTB (Day 7)
NOTCH1
HES1
TGFB2
TGFBR2
ID3
ASCL1
j
Number of regulated DEGs
Up
Down
1,844
1,037
87
Empty
LSD1-WT
LSD1-K661A
k
LSD1-KO + Empty
LSD1-KO + LSD1-WT
LSD1-KO + LSD1-K661A
DEG
non−DEG
Log2 (FC)
Average log2 expression in DMSO
l
Empty
LSD1-WT
LSD1-K661A
DMSO TAS1440 DMSO TAS1440 DMSO TAS1440
TGFB2
NOTCH1
NOTCH2
HES1
ID3
NOTCH3
ASCL1
Z-score
m
KEGG gene set enrichment analysis
NES
NOTCH signaling pathway
TGF-β signaling pathway
Pancreatic cancer
Lysine degradation
Propanoate metabolism
Melanoma
Glycerolipid metabolism
Pyruvate metabolism
Prostate cancer
Sphingolipid metabolism
Empty
LSD1-WT
LSD1-K661A
n
IP-FLAG
DMSO
TAS1440
3XFLAG-MYC
Empty
LSD1-WT
LSD1-K661A
FLAG-LSD1
INSM1
SMAD2

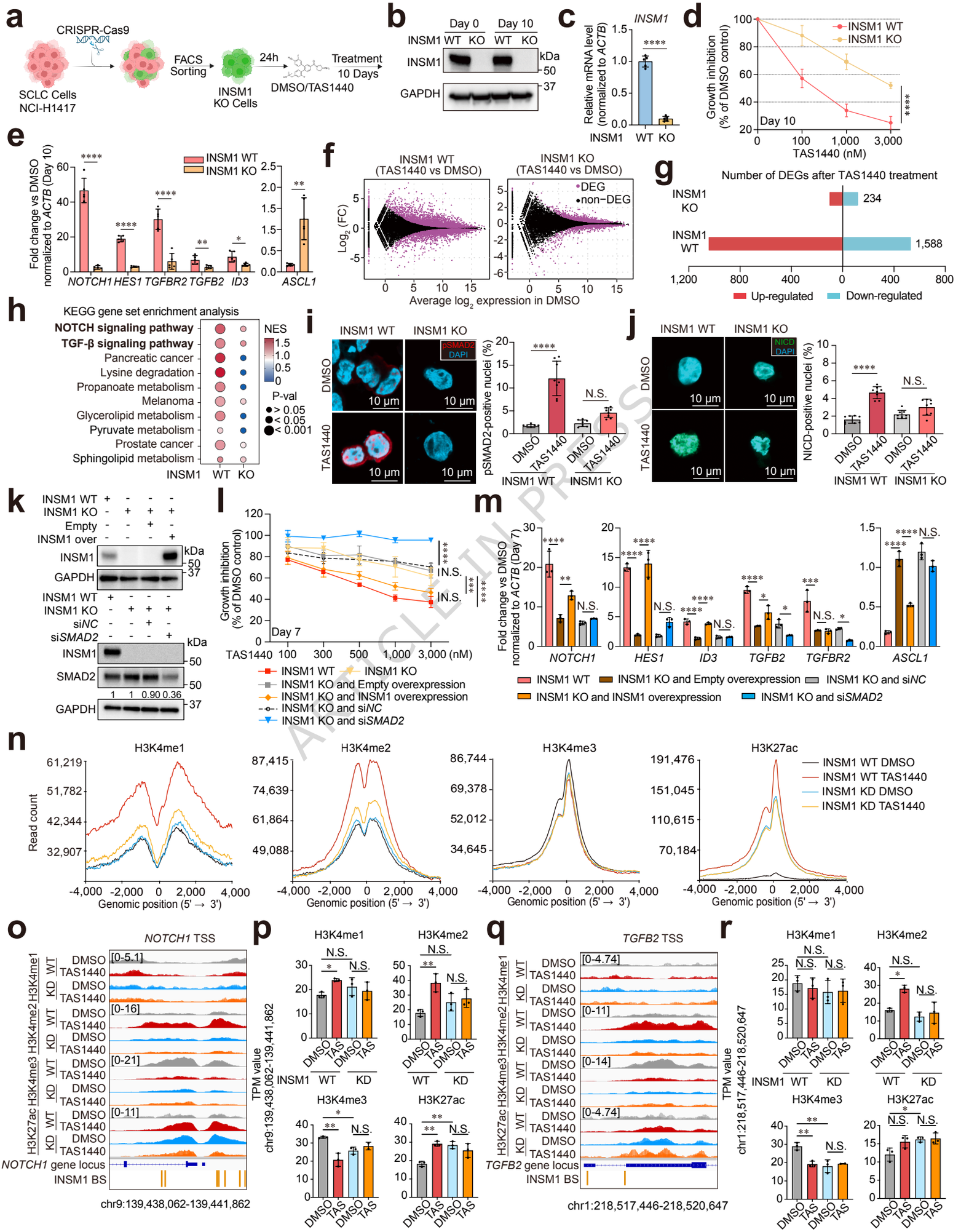
a
CRISPR-Cas9
SCLC Cells
NCI-H1417
FACS Sorting
INSM1 KO Cells
24h
Treatment 10 Days
DMSO/TAS1440
b
Day 0
Day 10
INSM1 WT KO WT KO
INSM1
GAPDH
kDa
50
37
c
INSM1
Relative mRNA level (normalized to ACTB)
INSM1 WT KO
d
INSM1 WT
INSM1 KO
Growth inhibition (% of DMSO control)
Day 10
TAS1440 (nM)
e
INSM1 WT
INSM1 KO
Fold change vs DMSO normalized to ACTB (Day 10)
NOTCH1 HES1 TGFBR2 TGFB2 ID3 ASCL1
f
INSM1 WT (TAS1440 vs DMSO)
INSM1 KO (TAS1440 vs DMSO)
DEG
non−DEG
Log2 (FC)
Average log2 expression in DMSO
g
Number of DEGs after TAS1440 treatment
INSM1 KO
INSM1 WT
234
1,588
Up-regulated
Down-regulated
h
KEGG gene set enrichment analysis
NOTCH signaling pathway
TGF-β signaling pathway
Pancreatic cancer
Lysine degradation
Propanoate metabolism
Melanoma
Glycerolipid metabolism
Pyruvate metabolism
Prostate cancer
Sphingolipid metabolism
NES
P-val
INSM1 WT KO
i
INSM1 WT
INSM1 KO
DMSO
TAS1440
pSMAD2
DAPI
10 μm
pSMAD2-positive nuclei (%)
N.S.
INSM1 WT
INSM1 KO
j
INSM1 WT
INSM1 KO
NICD
DAPI
NICD-positive nuclei (%)
k
INSM1 WT
INSM1 KO
Empty
INSM1 over
INSM1
GAPDH
siNC
siSMAD2
SMAD2
1 1 0.90 0.36
l
Growth inhibition (% of DMSO control)
Day 7
TAS1440 100 300 500 1,000 3,000 (nM)
INSM1 WT
INSM1 KO
INSM1 KO and Empty overexpression
INSM1 KO and INSM1 overexpression
INSM1 KO and siNC
INSM1 KO and siSMAD2
m
Fold change vs DMSO normalized to ACTB (Day 7)
NOTCH1 HES1 ID3 TGFB2 TGFBR2 ASCL1
INSM1 WT
INSM1 KO and Empty overexpression
INSM1 KO and siNC
INSM1 KO and INSM1 overexpression
INSM1 KO and siSMAD2
n
H3K4me1
H3K4me2
H3K4me3
H3K27ac
Read count
Genomic position (5' → 3')
INSM1 WT DMSO
INSM1 WT TAS1440
INSM1 KD DMSO
INSM1 KD TAS1440
o
NOTCH1 TSS
H3K4me1
H3K4me2
H3K4me3
H3K27ac
WT
KD
DMSO
TAS1440
NOTCH1 gene locus
INSM1 BS
chr9:139,438,062-139,441,862
p
H3K4me1
H3K4me2
H3K4me3
H3K27ac
TPM value
chr9:139,438,062-139,441,862
INSM1 WT KD
q
TGFB2 TSS
TGFB2 gene locus
INSM1 BS
chr1:218,517,446-218,520,647
r
H3K4me1
H3K4me2
H3K4me3
H3K27ac
TPM value
chr1:218,517,446-218,520,647
INSM1 WT KD

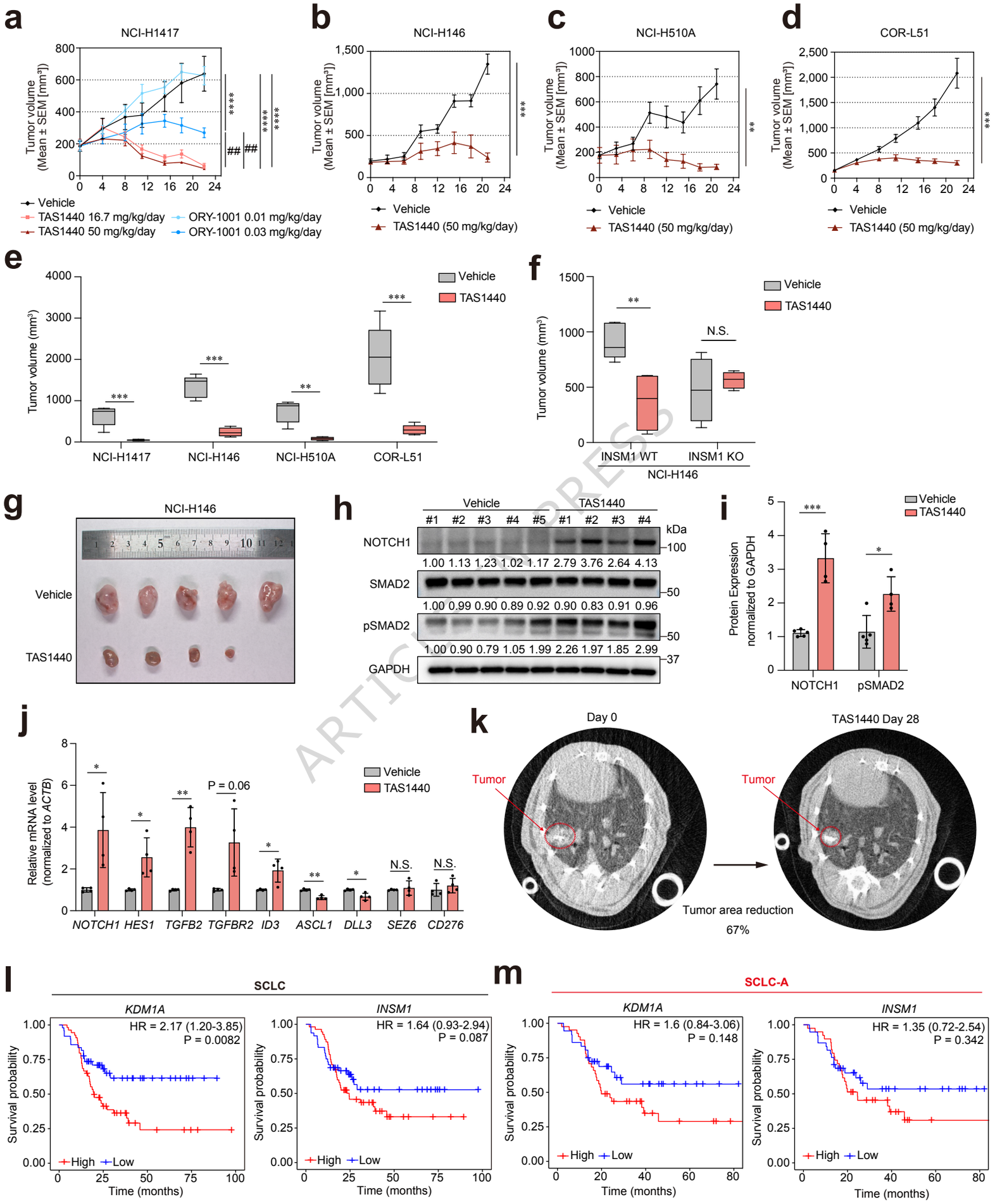
a
NCI-H1417
Tumor volume (Mean ± SEM [mm³])
Vehicle
TAS1440 16.7 mg/kg/day
TAS1440 50 mg/kg/day
ORY-1001 0.01 mg/kg/day
ORY-1001 0.03 mg/kg/day
b
NCI-H146
Vehicle
TAS1440 (50 mg/kg/day)
c
NCI-H510A
d
COR-L51
e
Tumor volume (mm³)
NCI-H1417
NCI-H146
NCI-H510A
COR-L51
f
INSM1 WT
INSM1 KO
N.S.
g
NCI-H146
Vehicle
TAS1440
h
NOTCH1
SMAD2
pSMAD2
GAPDH
kDa
i
Protein Expression normalized to GAPDH
j
Relative mRNA level (normalized to ACTB)
P = 0.06
NOTCH1 HES1 TGFB2 TGFBR2 ID3 ASCL1 DLL3 SEZ6 CD276
k
Day 0
TAS1440 Day 28
Tumor
Tumor area reduction
67%
l
SCLC
KDM1A
HR = 2.17 (1.20-3.85)
P = 0.0082
INSM1
HR = 1.64 (0.93-2.94)
P = 0.087
Survival probability
High
Low
Time (months)
m
SCLC-A
KDM1A
HR = 1.6 (0.84-3.06)
P = 0.148
INSM1
HR = 1.35 (0.72-2.54)
P = 0.342